THE ASTRONOMICAL JOURNAL, 122:2833–2849, 2001 December

A SURVEY OF $z > 5.8$ QUASARS IN THE SLOAN DIGITAL SKY SURVEY. I. DISCOVERY OF THREE NEW QUASARS AND THE SPATIAL DENSITY OF LUMINOUS QUASARS AT $z \sim 6$[1,2]

XIAOHUI FAN,[3] VIJAY K. NARAYANAN,[4] ROBERT H. LUPTON,[4] MICHAEL A. STRAUSS,[4] GILLIAN R. KNAPP,[4] ROBERT H. BECKER,[5,6] RICHARD L. WHITE,[7] LAURA PENTERICCI,[8] S. K. LEGGETT,[9] ZOLTÁN HAIMAN,[4,10] JAMES E. GUNN,[4] ŽELJKO IVEZIĆ,[4] DONALD P. SCHNEIDER,[11] SCOTT F. ANDERSON,[12] J. BRINKMANN,[13] NETA A. BAHCALL,[4] ANDREW J. CONNOLLY,[14] ISTVÁN CSABAI,[15,16] MAMORU DOI,[17] MASATAKA FUKUGITA,[18] TOM GEBALLE,[19] EVA K. GREBEL,[8] DANIEL HARBECK,[8] GREGORY HENNESSY,[20] DON Q. LAMB,[21] GAJUS MIKNAITIS,[12] JEFFREY A. MUNN,[22] ROBERT NICHOL,[23] SADANORI OKAMURA,[17] JEFFREY R. PIER,[22] FRANCISCO PRADA,[24] GORDON T. RICHARDS,[10] ALEX SZALAY,[15] AND DONALD G. YORK[21]

Received 2001 July 27; accepted 2001 August 28

ABSTRACT

We present the results from a survey of *i*-dropout objects selected from ~ 1550 deg^2 of multicolor imaging data from the Sloan Digital Sky Survey to search for luminous quasars at $z \gtrsim 5.8$. Objects with $i^* - z^* > 2.2$ and $z^* < 20.2$ are selected, and follow-up *J*-band photometry is used to separate L- and T-type cool dwarfs from high-redshift quasars. We describe the discovery of three new quasars, SDSSp J083643.85+005453.3 ($z = 5.82$), J130608.26+035626.3 ($z = 5.99$), and J103027.10+052455.0 ($z = 6.28$). The quasar SDSSp J083643.85+005453.3 is a radio source with flux of 1.1 mJy at 20 cm. The spectra of all three quasars show strong and broad Lyα + N v emission lines and very strong Lyα forest absorption, with a mean continuum decrement $D_A > 0.90$. The ARC 3.5 m spectrum of SDSSp J103027.10+052455.0 shows that over a range of ~ 300 Å immediately blueward of the Lyα emission, the average transmitted flux is only 0.003 ± 0.020 times that of the continuum level, consistent with zero flux over a ~ 300 Å range of the Lyα forest region and suggesting a tentative detection of the complete Gunn-Peterson trough. The existence of strong metal lines in the quasar spectra suggests early metal enrichment in the quasar environment. The three new objects, together with the previously published $z = 5.8$ quasar SDSSp J104433.04−012502.2, form a complete color-selected flux-limited sample at $z \gtrsim 5.8$. We estimate the selection function of this sample, taking into account the estimated variations in the quasar spectral energy distribution, as well as observational photometric errors. We find that at $z = 6$,

---

[1] Based on observations obtained with the Sloan Digital Sky Survey and with the Apache Point Observatory 3.5 m telescope, which is owned and operated by the Astrophysical Research Consortium; on observations obtained by staff of the Gemini Observatory, which is operated by the Association of Universities for Research in Astronomy, Inc., under a cooperative agreement with the National Science Foundation (NSF) on behalf of the Gemini partnership: the NSF (United States), the Particle Physics and Astronomy Research Council (United Kingdom), the National Research Council (Canada), CONICYT (Chile), the Australian Research Council (Australia), CNPq (Brazil), and CONICET (Argentina); on observations obtained at the W. M. Keck Observatory, which is operated as a scientific partnership among the California Institute of Technology, the University of California, and the National Aeronautics and Space Administration, made possible by the generous financial support of the W. M. Keck Foundation; on observations obtained at the German-Spanish Astronomical Centre, Calar Alto Observatory, operated by the Max Planck Institute for Astronomy, Heidelberg, jointly with the Spanish National Commission for Astronomy; and on observations obtained at UKIRT, which is operated by the Joint Astronomy Centre on behalf of the UK Particle Physics and Astronomy Research Council.

[2] This paper is dedicated to the memory of Arthur Davidsen, who was a pioneer of the study of the intergalactic medium and who showed great leadership as chairman of the Advisory Council of the Sloan Digital Sky Survey.

[3] Institute for Advanced Study, Olden Lane, Princeton, NJ 08540.
[4] Princeton University Observatory, Princeton, NJ 08544.
[5] Department of Physics, University of California at Davis, Davis, CA 95616.
[6] IGPP/Lawrence Livermore National Laboratory, Livermore, CA 95616.
[7] Space Telescope Science Institute, 3700 San Martin Drive, Baltimore, MD 21218.
[8] Max-Planck-Institut für Astronomie, Königstuhl 17, D-69171 Heidelberg, Germany.
[9] United Kingdom Infrared Telescope, Joint Astronomy Center, 660 North A'ohoku Place, Hilo, HA 96720.
[10] Hubble Fellow.
[11] Department of Astronomy and Astrophysics, Pennsylvania State University, University Park, PA 16802.
[12] Department of Astronomy, University of Washington, Box 351580, Seattle, WA 98195.
[13] Apache Point Observatory, P.O. Box 59, Sunspot, NM 88349-0059.
[14] Department of Physics and Astronomy, University of Pittsburgh, Pittsburgh, PA 15260.
[15] Department of Physics and Astronomy, Johns Hopkins University, 3400 North Charles Street, Baltimore, MD 21218.
[16] Department of Physics of Complex Systems, Eötvös University, H-1117 Budapest, Hungary.
[17] Department of Astronomy and Research Center for the Early Universe, School of Science, University of Tokyo, Hongo, Bunkyo, Tokyo 113-0033, Japan.
[18] Institute for Cosmic-Ray Research, University of Tokyo, Midori, Tanashi, Tokyo 188-8502, Japan.
[19] Gemini Observatory, 670 North A'ohoku Place, Hilo, HI 96720.
[20] US Naval Observatory, 3450 Massachusetts Avenue, NW, Washington, DC 20392-5420.
[21] Astronomy and Astrophysics Center, University of Chicago, 5640 South Ellis Avenue, Chicago, IL 60637.
[22] US Naval Observatory, P.O. Box 1149, Flagstaff Station, Flagstaff, AZ 86002-1149.
[23] Department of Physics, Carnegie Mellon University, Pittsburgh, PA 15213.
[24] Centro Astronómico Hispano Alemán, C/Jesús Durbán Remón 2-2, E-04004 Almería, Spain.

the comoving density of luminous quasars at $M_{1450} < -26.8$ ($H_0 = 50$ km s^{-1} Mpc^{-1}, $\Omega = 1$) is 1.1×10^{-9} Mpc^{-3}. This is a factor of ~ 2 lower than that at $z \sim 5$ and is consistent with an extrapolation of the observed quasar evolution at $z < 5$. Using the current sample, we discuss the constraint on the shape of the quasar luminosity function and the implications for the contribution of quasars to the ionizing background at $z \sim 6$. The luminous quasars discussed in the paper have central black hole masses of several times $10^9\ M_\odot$ by the Eddington argument, with likely dark halo masses on the order of $10^{13}\ M_\odot$. Their observed space density provides a sensitive test of models of quasar and galaxy formation at high redshift.

Key words: intergalactic medium — quasars: absorption lines — quasars: emission lines — quasars: general

1. INTRODUCTION

High-redshift quasars provide direct probes of the epoch when the first generation of galaxies and quasars formed. The absorption spectra of these quasars reveal the state of the intergalactic medium (IGM) close to the reionization epoch (Haiman & Loeb 1999; Miralda-Escudé, Haehnelt, & Rees 2000; Madau & Rees 2000; Cen & Haiman 2000). The lack of a Gunn-Peterson trough (Shklovsky 1964; Scheuer 1965; Gunn & Peterson 1965) in the spectrum of the luminous quasar SDSSp J104433.04−012502.2[25] at $z = 5.8$ (SDSS 1044−0125 for brevity—Fan et al. 2000c; for an updated redshift of this object, see Goodrich et al. 2001 and Djorgovski et al. 2001) indicates that the universe was already highly ionized at that redshift. Assuming that SDSS 1044−0125 is radiating at the Eddington luminosity, this object contains a central black hole of several billion solar masses. The assembly of such massive objects in a timescale shorter than 1 Gyr yields constraints on models of the formation of massive black holes (see, e.g., Haiman & Loeb 2001). The abundance and evolution of such quasars can provide sensitive tests for models of quasar and galaxy evolution.

The Sloan Digital Sky Survey (SDSS; York et al. 2000; Stoughton et al. 2001) uses a dedicated 2.5 m telescope and a large-format CCD camera (Gunn et al. 1998) at the Apache Point Observatory in New Mexico to obtain images in five broad bands (*u*, *g*, *r*, *i*, and *z*,[26] centered at 3551, 4686, 6166, 7480 and 8932 Å, respectively; Fukugita et al. 1996) over 10,000 deg^2 of high Galactic latitude sky. Over 200 quasars at $z > 3.5$ have been discovered to date from the SDSS multicolor imaging data (Fan et al. 1999a, 2000a, 2000c, 2001a; Zheng et al. 2000; Schneider et al. 2000, 2001; Anderson et al. 2001). The inclusion of the reddest band, *z*, in principle enables the discovery of quasars up to $z \sim 6.5$ from the SDSS data (Fan et al. 2000c).

Encouraged by the discovery of SDSS 1044−0125, we have carried out a systematic survey of *i*-dropout quasars ($z \gtrsim 5.8$, whose Lyα forest is entirely in the *i* band) based on the SDSS imaging data. The goals of this survey are (1) to define a color-selected flux-limited complete sample of quasars at $z \sim 6$ in order to study the evolution of the quasar spatial density at high redshift; (2) to provide multiple lines of sight for studying the nature of the high-redshift IGM; (3) to study the intrinsic properties of quasars and the metallicity of the quasar environment at high redshift.

In this paper, we present the first results of this survey, covering an area of 1550 deg^2. In § 2, we present our color selection procedures for $z > 5.8$ quasars. Special software is developed to control the number of false single-band detections in the imaging data. Follow-up optical and near-IR photometry is used to separate high-redshift quasar candidates from the more numerous cool dwarfs that have similar optical colors. In § 3, we describe the discovery of three new quasars at $z = 5.82$, 5.99, and 6.28. We discuss their spectral properties and the implications for the metallicity of the quasar environment and the status of the IGM in § 4. These three quasars, combined with SDSS 1044−0125, form a complete color-selected sample at $z^* < 20.2$. We calculate the survey selection function and derive the spatial density of $z \sim 6$ quasars in § 5. In § 6, we discuss the cosmological implications of the observations. Follow-up spectroscopic observations carried out with the Keck II telescope will be presented by Becker et al. (2001, hereafter Paper II).

We present our results using two different cosmologies throughout the paper: a Λ-dominated universe with $H_0 = 65$ km s^{-1} Mpc^{-1}, $\Lambda = 0.65$ and $\Omega = 0.35$ (Ostriker & Steinhardt 1995; Krauss & Turner 1995), which is referred to as the Λ-model; and an Einstein–de Sitter universe with $\Omega = 1$ and $H_0 = 50$ km s^{-1} Mpc^{-1}, which we refer to as the $\Omega = 1$ model in this paper. The age of the universe is 13.9 and 13.0 Gyr in the Λ-model and the $\Omega = 1$ model, respectively.

2. CANDIDATE SELECTION

2.1. *Colors of $z > 5.8$ Quasars*

The observed colors of quasars evolve strongly with redshift, as the intrinsic emission and the intervening absorption spectral features move through the SDSS filter system (Fan 1999; Richards et al. 2001a). The strong Lyα forest absorption blueward of the Lyα emission line enters the SDSS *g*, *r*, and *i* bands at redshifts of about 3.6, 4.6, and 5.5, respectively. At $z \gtrsim 5.7$, the Lyα emission line begins to move out of the SDSS *i* filter. With an average $i^* - z^* \gtrsim 2$, these high-redshift quasars have undetectable flux in the bluer *u*, *g*, and *r* bands and little flux (sometimes also undetectable) in *i* band. They become *i*-dropout objects with only one measurable color in SDSS photometry.

Figure 1 presents the $i^* - z^*$ versus z^* color-magnitude diagram for 50,000 stellar sources selected at random from the SDSS imaging data. It also shows the locations of all the *i*-dropout objects (including L/T dwarfs and high-redshift quasars; see below) selected in the 1550 deg^2 survey area. The median track of simulated quasars (see § 5.1) with absolute magnitude $M_{1450} = -27$, representative of the quasars

[25] The naming convention for the SDSS sources is SDSSp JHHMMSS.SS±DDMMSS.S, where "p" stands for the preliminary SDSS astrometry, and the positions are expressed in J2000.0 coordinates. The astrometry is accurate to better than 0".2 in each coordinate.

[26] Following Stoughton et al. 2001, we refer to the SDSS passbands as *u*, *g*, *r*, *i*, and *z*. As the SDSS photometric calibration system is still being finalized, the SDSS photometry presented here is referred to as u^*, g^*, r^*, i^* and z^*.

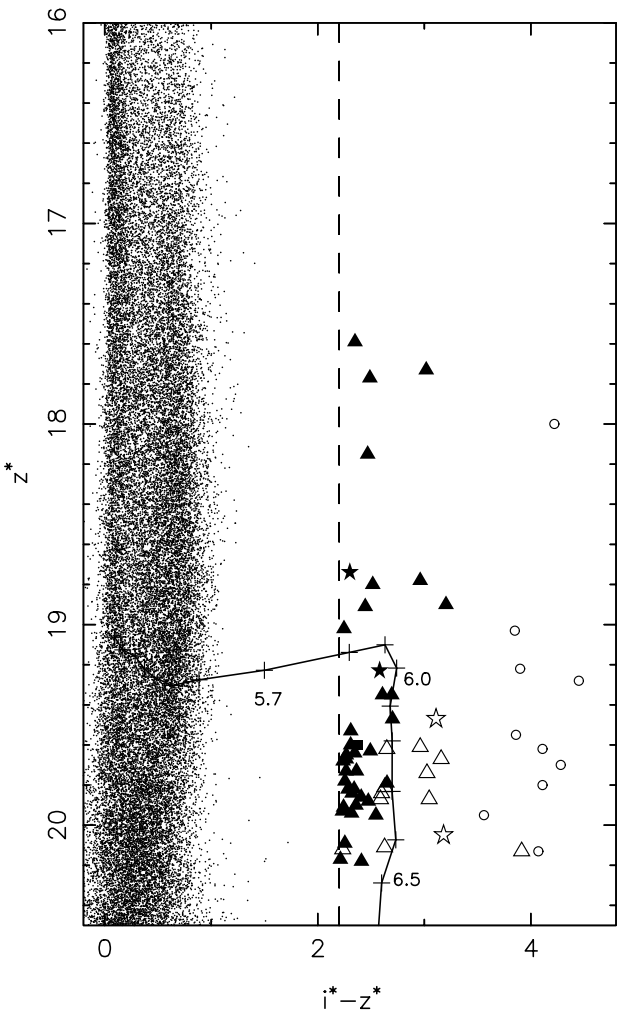

FIG. 1.—The i^*-z^* vs. z^* color-magnitude diagram for the i-dropout sample. Colors and magnitudes are plotted as asinh magnitudes measured by SDSS imaging. The symbols represent the classification in Table 2 (*circles*: T dwarfs, *triangles*: L dwarfs; *stars*: $z > 5.8$ quasars; *square*: BAL quasar). Filled symbols are objects with S/N in the i band higher than 4; open symbols are objects not detected in the i band at the 4 σ level. The median track of simulated i^*-z^* color and z^* magnitude for quasars with $M_{1450} = -27$ is also shown as a function of redshift, with plus signs every 0.1 in redshift. For comparison, the data for a random sample of 50,000 high-latitude stars are also shown as dots. The dashed line shows the cut $i^*-z^* > 2.2$ that we use to select high-redshift quasar candidates.

discussed in this paper, is also plotted. A simple cut at $i^*-z^* > 2.2$ selects quasar candidates at $z > 5.8$. At $z > 6.0$, the Lyα forest absorption enters the z filter, and the z^* flux decreases rapidly with redshift with increasing amount of absorption, while i^*-z^* remains approximately constant, as the increasing absorption in the i and z bands are roughly equal. At $z \sim 6.6$, the Lyα emission line has redshifted to 9240 Å, well past the effective wavelength of the z filter. Most of the z flux is absorbed by the Lyα forest, and the object disappears from optical images altogether. This is the upper limit to the redshift of objects detectable with SDSS imaging data.

Quasars at $z > 5.8$ are extremely rare on the sky. We found four i-dropout quasars in 1550 deg^2. For comparison, over the same area, there are about 15 million objects detected in the z band above 6 σ, and about 6.5 million cosmic-ray hits in the z band. The quasars are faint, with low signal-to-noise ratio (S/N) photometry from the SDSS imaging data. Therefore, the key to a successful selection process is an efficient elimination of potential contaminants. We face three technical challenges:

1. Eliminating false z-band–only detections, composed primarily of cosmic rays, but also including satellite trails, electronic ghost images and bleed trails from bright stars. While the recognition of the majority of cosmic rays is relatively straightforward, even a tiny fraction of misclassified cosmic rays in the z band, which would then appear as i-dropout candidates, would dominate over the much rarer true quasars. Note that SDSS scans the sky only once in the course of the survey except in a small fraction of overlapping area; thus, repeat observations cannot be used to recognize cosmic rays. Moreover, SDSS uses thick CCDs for the z band. A cosmic-ray hit on these thick devices typically occupies more than a single pixel, making the separation of real detections from cosmic-ray hits more difficult, especially when the seeing is good.

2. Obtaining reliable z^* photometry. As is evident from Figure 1, the i-dropout objects are distributed on the extreme tail of the i^*-z^* distribution. Under typical seeing, $\sigma(z^*) \sim 0.1$ for objects with $z^* \sim 20$. Objects in the tail of the error distribution could scatter into the selected region of color space and pose a serious contamination when a large number of objects is searched.

3. Separating quasars and cool dwarfs. As shown in § 3, the surface density of cool dwarfs, with spectral types ranging from mid-L to T, which have $i^*-z^* > 2.2$ (Geballe et al. 2001; Leggett et al. 2001), is $\sim$15 times higher than that of $z > 5.8$ quasars. We use J-band photometry to separate these two classes of objects (see below; see also Fan et al. 2000b; Zheng et al. 2000).

2.2. *Selection Procedure*

Because of the rarity of high-redshift quasars and the overwhelming number of contaminants, our photometric selection procedure of $z > 5.8$ quasar candidates is quite involved and includes five separate steps, as follows:

1. selection of i-dropout sources from the SDSS database;
2. running an improved cosmic-ray classifier and visually inspecting all remaining candidates to reduce the number of false candidates due to cosmic rays;
3. matching the candidate list to the Two Micron All Sky Survey (2MASS; Skrutskie et al. 1997) in the public-release area of 2MASS to obtain JHK photometry;
4. independent z-photometry to further eliminate false and biased z-detections;
5. J-band photometry of objects not in 2MASS to separate quasar and cool dwarf candidates.

This then leaves us with a sample for follow-up spectroscopy.

In this and the subsequent section, we describe this process in detail. The techniques and rationale for these various cuts are described in the present section, while the observations themselves are described in § 3.

2.2.1. *Selection of i-Dropout Objects from SDSS Imaging Data*

The SDSS photometric data are processed by a series of automated pipelines to carry out astrometric and photometric measurements. The photometric pipeline (PHOTO, Lupton et al. 2001) reduces the data from the imaging

camera and produces corrected images and object catalogs. PHOTO classifies detected objects either as "star" (point source, consistent with the point-spread function, or PSF) or "galaxy" (extended source). However, we select all *i*-dropout objects irrespective of their star-galaxy classification, as the star-galaxy separation becomes less reliable at the low S/N level. Cosmic rays are recognized as objects with profile gradients significantly steeper than that of the PSF and are interpolated over; they are not output explicitly by the pipeline. While PHOTO classifies more than 99.9% of the cosmic rays correctly, visual inspection shows that a majority of objects with *z*-only detections that are classified as "stars" still have the appearance of cosmic rays. This is further confirmed by comparing those areas of the sky with multiple observations. Therefore, we have recently improved the performance of the object classifier, as follows.

For every object detected by the imaging pipeline, we count the pixels in an 11 × 11 pixel region (4.″4 × 4.″4) centered on the object, for which

$$\frac{\mathrm{PSF}\,(d)}{\mathrm{PSF}\,(0)} > \frac{I(d) + cN[I(d)]}{I(0) - cN[I(0)]}\,, \qquad (1)$$

where $I(0)$ is the object's central intensity, $I(d)$ is the intensity of the pixel in question, PSF (0) and PSF (d) are the equivalent quantities for the locally determined model of the PSF, the noise N is the photon noise with an additional $0.05I(0)$ added in quadrature, and $c = 1.5$. This criterion searches for objects with profile gradients significantly sharper than that of the PSF. If more than 3 pixels satisfy this condition, we consider the object to be a candidate cosmic ray and reject it.

The photometric pipeline assigns detailed flags for each detected object, indicating objects whose photometry (and, therefore, colors) may be in error. We reject objects flagged as being saturated in any band, lying on the bleed trail of a saturated star, or overlapping the edge of the image boundary. We pay close attention to objects blended with close neighbors and reject deblended children with PEAKCENTER, NOTCHECKED, or DEBLEND_NOPEAK set in the *i* and *z* bands, which are typical signs of deblending problems. (For a complete description of the definition of flags, see Stoughton et al. 2001.) The flag-checking procedure used here is similar to that used in the SDSS quasar target selection pipeline (Richards et al. 2001b).

We have reclassified all the objects with $i^* - z^* > 2.2$ using the new cosmic-ray classifier. We found that depending on the seeing of a specific run, roughly 50%–70% of the *i*-dropout objects formerly classified as "stars" are now classified as cosmic rays, while a negligible fraction of the "real" objects (based on multiple observations and objects with confirmed spectra) are misclassified as "cosmic rays." We then visually inspect the *z* images of the remaining candidates and reject a further 25% as cosmic rays and other artifacts.

After the improved cosmic-ray rejection and visual inspection, we carry out independent follow-up *z* photometry of all the remaining candidates (of which there are 121; see below) using the Apache Point 3.5 m and other telescopes (see § 3.1). This serves two purposes: (1) to confirm that the objects are indeed real and (2) to measure the z^* magnitude more accurately. Since our *i*-dropout candidates have the reddest $i^* - z^*$ colors, we tend to pick up objects lying on the several-σ tail of the z^* error distribution (note that the *z*-band–only objects are very faint and therefore are measured at low S/N); they will thus have artificially red $i^* - z^*$ color and blue $z^* - J$ color and are more likely to be selected as $z > 5.8$ quasar candidates (see below). To include those objects in the sample would lower our spectroscopic success rate considerably.

2.2.2. *Near-IR Photometry: Separating Quasars and L/T Dwarfs*

As discussed by Fan et al (2000b) and Zheng et al. (2000) and illustrated in Figure 1, the major astrophysical contaminants of *i*-dropout quasars are very cool dwarfs with spectral types L and T (Strauss et al. 1999; Tsvetanov et al. 2000; Fan et al. 2000a; Leggett et al. 2000, 2001; Geballe et al. 2001). These have effective temperatures $T_{\rm eff} < 1800$ K and $i^* - z^* > 2$, and they cannot be distinguished from $z > 5.8$ quasars using SDSS optical photometry alone. Figure 2 presents the $i^* - z^*$ versus $z^* - J$ color-color diagram of the *i*-dropout sample. Finlator et al. (2000) have matched the SDSS photometric catalog in ~ 50 deg^2 with that of 2MASS in the *JHK* bands. The small dots in Figure 2 show the SDSS-2MASS matches and indicate the location of normal stars on this color-color diagram. The track of quasar colors shows that by using $z^* - J < 1.5$, *i*-dropout cool dwarfs and high-redshift quasars are clearly separated, as the $z^* - J$ color of high-redshift quasars is dominated by the blue power-law continuum, while the cool temperature of L/T dwarfs results in very red $z^* - J$ color, typically larger than 2. Therefore we determine whether the candidate has been detected by 2MASS. While the nondetection of a faint candidate by 2MASS does not give a tight constraint on the spectral shape of the object, most of the brighter objects ($z^* < 19$) that are located in the area of the 2MASS publicly released data are indeed detected by

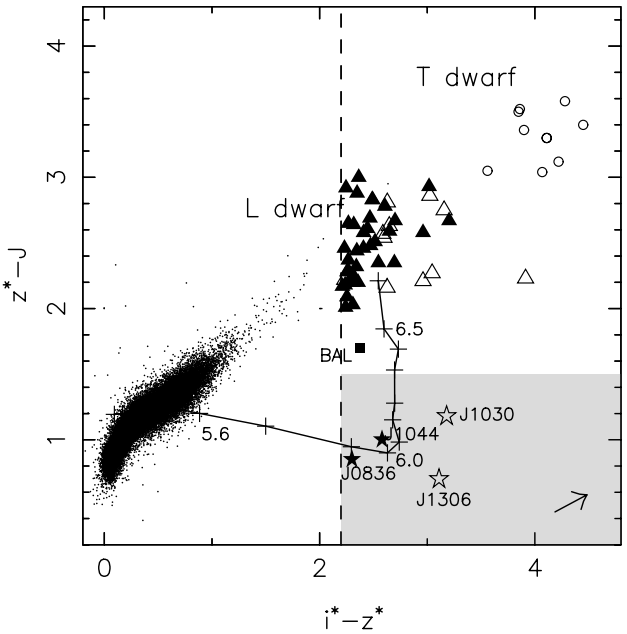

FIG. 2.—The $i^* - z^*$ vs. $z^* - J$ color-color diagram for the *i*-dropout sample. The symbols are the same as in Fig. 1. The median track of simulated quasar colors is shown as a function of redshift. The survey selection criteria are illustrated by the shaded area. For comparison, colors of SDSS-2MASS stars in a 50 deg^2 area at high latitude are also shown. The arrow at the lower right corner indicates the reddening vector for quasars at $z = 6$ with $E(B-V) = 0.1$.

2MASS, with $z^* - J \gtrsim 2$, indicating that most of them are cool dwarfs. For those not matched with 2MASS, we carry out follow-up J-band photometry (see § 3.1).

2.2.3. *Color Selection Criteria*

The final photometric selection criteria for this survey are

$$z^* < 20.2\ , \tag{2a}$$

$$\sigma(z) < 0.1\ , \tag{2b}$$

$$i^* - z^* > 2.2\ , \tag{2c}$$

$$z^* - J < 1.5\ . \tag{2d}$$

We also require that the object not be detected in any of the other three bands, u, g, and r.

The magnitudes and colors in equation (1) are *not* corrected for interstellar extinction. This is a small effect, which has been taken into account in the selection function calculation (§ 5.1). In the selection, only objects with S/N > 10 in the z band are considered (eq. [2b]), as the $i-z$ color becomes very unreliable for the faintest sources and would have selected many more candidates with a more inclusive cut. Equation (2c) selects quasars with $z \gtrsim 5.8$, and equation (2d) separates quasars from cool dwarfs. Note that the SDSS photometry is on the AB magnitude system (Fukugita et al. 1995), while the J-band photometry is on the Vega-based system. The selected area is illustrated as the shaded region in Figure 2.

3. DISCOVERY OF THREE NEW QUASARS

3.1. *Photometric Observations*

Table 1 lists the details of the 25 SDSS photometric runs used in this survey. The projection of these runs on the sky is illustrated in Figure 3. The entire region is located in the northern Galactic cap. In Table 1, the location of each run is presented in terms of survey stripe number (n) and the range of survey great-circle longitude ($\lambda_{\rm min}$ and $\lambda_{\rm max}$). When taking data, the SDSS telescope moves along a series of great circles on the sky and the photometric camera drift-scans at the sidereal rate, with an effective exposure time of 54.1 s. The survey coordinate system (λ, η) is a spherical system with poles at $\alpha = 95°$ and 275°, $\delta = 0°$ (J2000.0). The point $(\lambda = 0°, \eta = 0°)$ is located at $\alpha = 185°$, $\delta = 35°$ (York

TABLE 1

SUMMARY OF PHOTOMETRIC RUNS

Run	Strip	$\lambda_{\rm min}$	$\lambda_{\rm max}$	$\langle$FWHM(i)$\rangle$ (arcsec)	$\langle$FWHM(z)$\rangle$ (arcsec)
745.....	10 N	51.1	65.0	1.23	1.25
752.....	10 S	−17.6	51.0	1.43	1.50
756.....	10 N	−63.1	51.0	1.34	1.38
1140.....	9 N	−30.5	17.1	1.44	1.47
1231.....	9 S	−14.2	14.7	1.51	1.53
1239.....	10 S	−63.1	−39.7	1.41	1.46
1241.....	9 S	−45.0	−38.9	1.49	1.57
1241.....	9 S	−24.8	−19.0	1.74	1.76
1331.....	36 S	−56.4	−36.0	1.18	1.18
1331.....	36 S	−30.2	−18.0	1.38	1.36
1332.....	36 S	−18.1	−10.2	1.52	1.46
1336.....	42 N	23.4	36.1	1.51	1.50
1339.....	42 S	23.3	36.0	1.41	1.38
1345.....	36 N	−52.6	−8.0	1.42	1.42
1345.....	36 N	1.3	73.9	1.23	1.26
1350.....	37 S	−53.7	14.5	1.54	1.54
1356.....	43 N	22.8	36.5	1.64	1.62
1359.....	43 S	27.7	37.2	1.61	1.57
1402.....	37 N	−51.0	−34.1	1.24	1.22
1412.....	37 N	−23.6	33.2	1.28	1.28
1449.....	1 N	2.9	13.4	1.46	1.51
1450.....	37 N	−34.2	−23.3	1.53	1.54
1462.....	11 S	−56.1	40.6	1.27	1.35
1468.....	32 N	10.4	29.1	1.37	1.35
1469.....	32 S	7.5	29.4	1.49	1.48
1478.....	12 S	25.6	55.8	1.43	1.49
2074.....	35 S	−34.6	−25.2	1.51	1.56
2076.....	35 N	−56.2	−33.9	1.33	1.35
2078.....	36 S	−9.4	8.5	1.47	1.49
2125.....	12 S	−64.5	−17.1	1.53	1.58
2126.....	12 N	−64.2	0.2	1.30	1.36
2131.....	34 S	−60.3	−42.6	1.41	1.50
2134.....	36 S	8.4	23.5	1.48	1.41
2137.....	34 N	−59.3	−19.6	1.37	1.43
2138.....	34 N	−22.7	−9.5	1.51	1.55
2140.....	34 S	−45.4	−35.3	1.69	1.76
2141.....	10 S	−38.0	−17.2	1.42	1.51
2190.....	12 N	2.3	28.2	1.47	1.54
2190.....	12 N	32.9	51.7	1.48	1.53

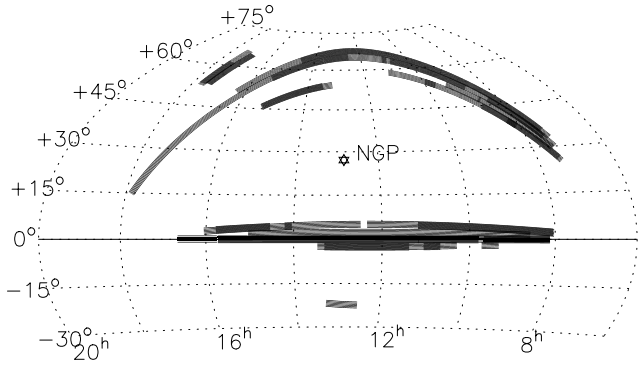

FIG. 3.—Projection of the survey area in J2000.0 equatorial coordinates. Note that for some SDSS stripes only one of the two scans is covered by the current survey. The stripes are each 2.°5 wide.

et al. 2000; Stoughton et al. 2001). Each drift scan tracks a survey stripe n centered on a constant η, given by

$$\eta = (n - 10) \times 2.^\circ5 - 32.5 . \quad (3)$$

Two scans, or strips, one offset to the north and one to the south, are required to fill a stripe. The 25 SDSS imaging runs used in the i-dropout survey in this paper were taken between 1999 March 20 (run 745) and 2001 March 19 (run 2190) over a range of seeing conditions. The seeing of SDSS images is characterized by the parameter psfWidth, defined as the effective width of the best-fit double-Gaussian PSF model. For a single-Gaussian profile, psfWidth = 1.06 FWHM. Only those runs, or parts of runs, with psfWidth in z band in the fourth column of the SDSS camera (near the middle of the focal plane) better than 1.″8 are used in this paper. The median seeing values (over all six columns of the camera) in the i and z bands are also listed in Table 1. Because of the complicated geometry of the survey and overlap between runs, we estimated the total survey area by Monte Carlo integration—calculating the fraction of randomly distributed points on the celestial sphere falling into the boundary of any of the runs listed in Table 1. The total area covered is 1550 deg^2, excluding regions with poor seeing. The median psfWidth is $\sim$1.″5 in the i and z bands over the whole area.

Following the procedures described in § 2, we first search the SDSS database and eliminate false detections (steps 1 and 2) based on the SDSS images. This results in a total of 121 objects with $i^* - z^* > 2.2$ that require further z- and J-band photometry. The candidate list includes five known T dwarfs from the SDSS (Strauss et al. 1999; Tsvetanov et al. 2000; Leggett et al. 2000), one known T dwarf from 2MASS (Burgasser et al. 1999), and the known $z = 5.8$ quasar SDSS 1044−0125. Thirty-five objects are located in the 2MASS first and second incremental data release area. Of these, 13 objects are detected in 2MASS JHK photometry and have colors of L to T dwarfs.

Independent z-photometry (step 4 in § 2.2) was carried out using the Seaver Prototype Imaging camera (SPICAM) in the SDSS z filter on the ARC 3.5 m telescope at the Apache Point Observatory in several nights between 2001 February and April. SPICAM has a back-side–illuminated SITe 2048 × 2048 pixel CCD with a field of view of 4.′8. The pixel scale is 0.″14, and the typical seeing was 1″. The quantum efficiency peaks at 89% at 6500 Å and is about 49% at 9000 Å. The exposure times were between 90 and 180 s, depending on the weather conditions. Note that since the SDSS photometry itself provides many local reference stars, photometric weather is not required for z photometry. The S/N is typically twice that of the SDSS imaging. The SPICAM images are reduced using normal IRAF procedures. Sky flats are constructed from the scaled median of target images. The z^* magnitudes are measured with aperture photometry with a radius of $\sim$2″ and calibrated by local SDSS standards.

Follow-up J-band infrared photometry (step 5 in § 2.2) was carried out on photometric nights using several telescopes, between 2001 February and May. The majority of the targets were observed with the GRIM II instrument (the near-IR grism spectrometer and imager), also on the ARC 3.5 m. It uses a 256 × 256 HgCdTe detector and covers a field of view of 1′ at f/10. JHK standards from Persson et al. (1998) were monitored throughout the night. We used similar IRAF procedures to reduce the GRIM II data. A small number of objects were observed with the UFTI instrument, a near-IR camera with a 1024 × 1024 HgCdTe detector covering 92″ × 92″ on the 3.8 m UK Infrared Telescope (UKIRT) on Mauna Kea, and with the MAGIC instrument, a near-IR imager and low-resolution infrared spectrograph at the 2.2 m telescope at Calar Alto Observatory in Spain. The typical photometric error of our infrared photometry is 0.05–0.10 mag and is dominated by calibration errors. Since quasars and L/T dwarfs have $z^* - J$ colors that differ by more than 0.5 mag, this error has very little effect on the selection efficiency (§ 5.2).

We attempted to follow the sequence described in § 2.2 to select i-dropout quasar candidates. But as we had to use photometric nights for the IR photometry, we changed the observing sequence in two cases: (1) on a dry photometric night, IR photometry had the highest priority; (2) when the weather was nonphotometric, for objects that had SPICAM z-photometry but did not yet have J-band photometry, we carried out spectroscopy directly, without preselection using $z^* - J$ color. In the latter case, we started from either the brightest or the reddest object, depending on weather. It is worth noting that the rapid instrument-change mechanism at the ARC 3.5 m ($\sim$15 minutes) and the excellent weather monitoring system at APO allow a very efficient use of telescope time. In the end, we obtained photometry and/or spectroscopy of our full sample.

3.2. *Spectroscopic Observations*

Table 2 summarizes the classifications of the i-dropout sample. Using 2MASS matches and follow-up z and J photometry, we found that among the 121 i-dropout candidates, 35 are false detections, most likely cosmic rays that still passed the first two steps of selection; 71 have

TABLE 2

SUMMARY OF FOLLOW-UP RESULTS

Parameter	No. Objects	Percentage
$z > 5.8$ quasars	4	3.3
T dwarfs	11	9.1
M/L dwarfs by spectroscopy	10	8.3
M/L dwarfs by photometry	60	49.6
BAL quasar	1	0.8
False detection	35	28.9
Total	121	100

$z^* - J > 2$ and are classified as cool dwarfs. Ten objects are classified as cool dwarfs based on spectroscopy, so no J photometry was necessary. The spectra of these dwarfs were obtained using the Double Imaging Spectrograph (DIS) on the ARC 3.5 m between 2001 March and May and using the Echelle Spectrograph and Imager (ESI) on the Keck II telescope in 2001 March. One of the candidates, SDSSp J081948.97+420930.2, has an intermediate $z^* - J$ color ($z^* - J = 1.7$); it is a low-ionization broad absorption line (BAL) quasar at $z = 2.05$ (see Becker et al. 1997; Hall et al. 2001). The Keck spectrum of this object is presented in Hall et al. (2001). Finally, four objects have $i^* - z^* > 2.2$ and $z^* - J < 1.5$, including the previously known $z = 5.8$ quasar SDSS 1044−0125 and three new quasars at $z > 5.8$. Note that in this survey *all* objects that satisfy the color selection criteria (eq. [1]) indeed turn out to be $z \gtrsim 5.8$ quasars from their spectra. The magnitude and colors of these objects are plotted on Figures 1 and 2.

Among the cool dwarfs found in this survey, eleven are T dwarfs. They form a complete flux-limited T dwarf sample. Six of these objects were previously known; the optical-IR spectra of four more of them are presented in Geballe et al. (2001). In a separate paper, we will present the photometry of L and T dwarfs in the i-dropout sample, the observations of the final T dwarf, and the analysis of the surface density and spatial densities of T dwarfs in the solar neighborhood.

The optical spectra of the three new quasars were obtained using the DIS on the ARC 3.5 m between 2001 March and May. The instrument and data reduction procedure are described in detail by Fan et al. (1999a). Figure 4 presents the z-band finding charts of the three new quasars, SDSSp J083643.85+005453.3 ($z = 5.82$; SDSS 0836+0054 for brevity), SDSSp J130608.26+035636.3 (SDSS 1306+0356, $z = 5.99$), and SDSSp J103027.10+052455.0 (SDSS 1030+0524, $z = 6.28$). Table 3 presents their photometric properties, and Figure 5 shows the ARC 3.5 m dis-

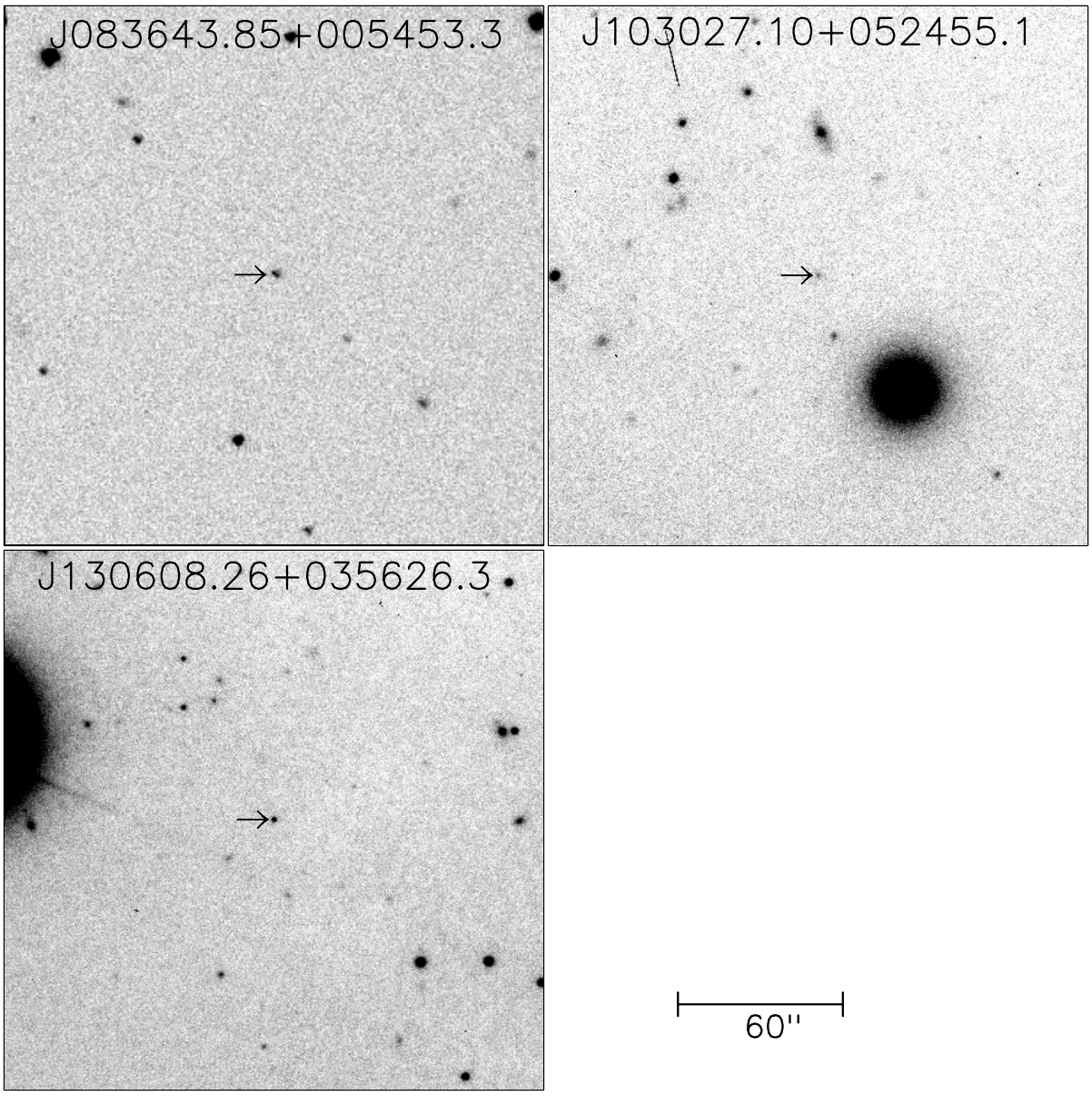

FIG. 4.—The z finding charts of the three new $z > 5.8$ quasars. For SDSS 0836+0054, the SDSS z image is shown. For SDSS 1030+0524 and SDSS 1306+0356, the ARC 3.5 m z images taken with SPICAM are shown (180 s exposure). The size of the finding chart is 160″. North is up, and east to the left.

TABLE 3

PHOTOMETRIC PROPERTIES OF THREE NEW $z > 5.8$ QUASARS

Object	Redshift	i^*	z^*	J	SDSS Run
J083643.85+005453.3.....	5.82 ± 0.02	21.04 ± 0.08	18.74 ± 0.05	17.89 ± 0.05	1239
J103027.10+052455.0.....	6.28 ± 0.03	23.23 ± 0.43	20.05 ± 0.10	18.87 ± 0.10	2125
J130608.26+035626.3.....	5.99 ± 0.03	22.58 ± 0.26	19.47 ± 0.05	18.77 ± 0.10	2190

NOTE.—The SDSS photometry (i^*, z^*) is reported in terms of *asinh magnitudes* on the AB system. The asinh magnitude system is defined by Lupton, Gunn, & Szalay (1999); it becomes a linear scale in flux when the absolute value of the signal-to-noise ratio is less than about 5. In this system, zero flux corresponds to 24.4 and 22.8, in i^* and z^*, respectively; larger magnitudes refer to negative flux values. The J magnitude is on the Vega-based system.

covery spectra of the three objects. The exposure time of each spectrum is 3600 s. The spectra in Figure 5 have been smoothed to a resolution of ~20 Å. The flux calibration has been adjusted to match the SDSS z^* magnitudes. The locations of the Lyα and N V emission lines are indicated in the figure. The expected positions of Lyβ + O VI and the Lyman limit are also shown.

A near-IR spectrum of SDSS 1030+0524 was obtained on the night of 2001 June 11, using the NIRSPEC (McLean et al. 1998) instrument on the Keck II Telescope, as part of the Gemini/NIRSPEC service observing program, carried out by Gemini staff scientists T. Geballe and M. Takamiya. Observations were taken in grating mode, with the N2 blocking filter and a 0.″76 slit, which gives a wavelength coverage of 1.09–1.29 μm and a spectral resolution of ~1500. A total of 10 exposures, each with 300 s exposure time, were taken using an ABBA sequence, nodding along the slit. The weather was photometric with ~0.″7 seeing. HIP 48414, a bright A1 V star, was observed as an atmospheric calibration star at similar air mass to that of the quasar observation. The NIRSPEC data were reduced using the WMKONSPEC package, an IRAF package developed at Keck Observatory to reduce NIRSPEC data. The flux calibration has been adjusted to match its measured J-band magnitude. The final reduced spectrum, binned to 4 Å pixel^{-1}, is shown in Figure 6. For comparison, the optical spectrum of SDSS 1030+0524 is also shown, and the locations of the Lyα, N V, and C IV emission lines are indicated.

4. SPECTRAL PROPERTIES

The discovery spectra of the three objects show unambiguous signatures of very high redshift quasars, similar to that of SDSS 1044−0125: strong, broad, and asymmetric Lyα + N V emission lines, with sharp discontinuities to the blue side, due to the onset of very strong Lyα absorption. The discovery spectra are of relatively low S/N. Accurate redshift determination from these spectra is difficult. The Lyα emission line is severely affected by the Lyα forest absorption, and the N V line is blended with Lyα. The low S/N does not allow us to use weaker lines such as O I + Si II λ1302 or Si IV + O IV] λ1400 to determine an accurate redshift. The next strong emission line in the quasar spectrum is C IV λ1549, which is located beyond 1 μm for $z > 5.5$ and requires near-IR spectroscopy. Therefore, we use the near-IR spectrum to determine the redshift of SDSS

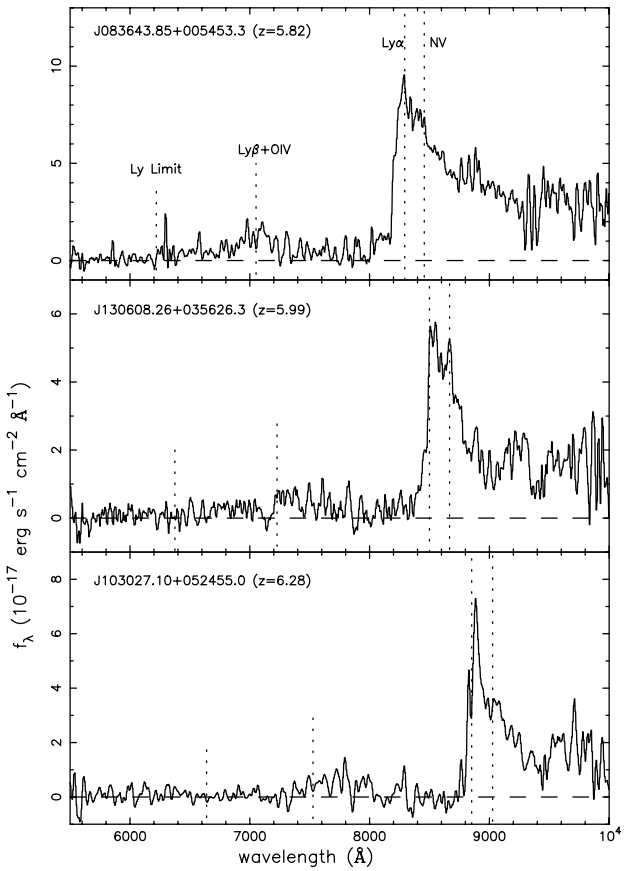

FIG. 5.—The discovery spectra of the three new $z > 5.8$ quasars, taken with the ARC 3.5 m telescope and DIS spectrograph. The exposure time is 3600 s for each quasar and the spectral resolution is about 20 Å. The spectra have been normalized to the photometry in the z filter.

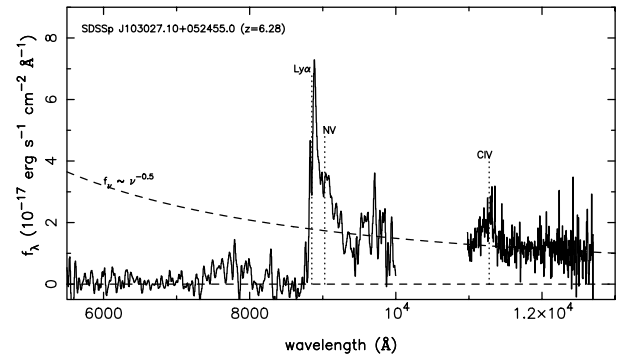

FIG. 6.—Combined optical+near-IR spectrum of SDSS 1030+0524. The optical spectrum is a 3600 s exposure taken with ARC 3.5 m telescope (same as in Fig. 5). The near-IR spectrum is a 3000 s exposure taken with Keck/NIRSPEC. The resolution of the near-IR spectrum is $R \sim 1500$.

1030+0524. The redshifts of the other two quasars were determined using high-S/N Keck spectra described in Paper II. The uncertainties in all these redshifts are of order 0.02. In this section, we first briefly comment on the major spectral signatures of each quasar (§ 4.1). We use the emission lines to constrain the metallicity of the quasar environment (§ 4.2). Then we calculate the average absorption in the Lyα forest region based on the discovery spectra and comment on the possible detection of the Gunn-Peterson trough in the spectrum of SDSS 1030+0524 (§ 4.3).

4.1. *Notes on Individual Objects*

SDSSp J083643.85+005453.3 ($z = 5.82$): This quasar has a similar redshift to SDSS 1044−0125. The Lyα emission line is very broad and strong. A separate N v λ1240 component is tentatively detected. The rest-frame equivalent width (EW) of the Lyα + N v line is ∼70 Å, quite typical of lower redshift quasars (Fan et al. 2001b). The Lyβ + O vi emission line is also clearly detected at ∼7000 Å; this line was also seen in the spectrum of SDSS 1044−0125. It is evident that there is detectable flux blueward of the Lyα emission line. The universe is still highly ionized at $z \sim 5.8$.

SDSS 0836+0054 is an extremely luminous object. With $z^* = 18.74$ and $J = 17.89$, it has an absolute magnitude $M_{1450} = -27.62$ ($\Omega = 1$ model; see § 5.1) and is the most luminous quasar discovered at $z > 4.5$ to date; in particular, it is 0.5 mag more luminous than SDSS 1044−1025. SDSS 0836+0054 has a radio counterpart in the FIRST radio survey (Becker, White, & Helfand 1995) at 20 cm. The radio source is unresolved with a total flux of 1.11 ± 0.15 mJy, and the positional match is better than 1″. This is the highest redshift radio-loud quasar known and the second radio-loud quasar detected at $z > 5$ (the other one is SDSSp J091316.56+591921.5 at $z = 5.11$, with a 20 cm flux of 18.1 mJy; see Anderson et al. 2001).

SDSSp J130608.26+035636.3 ($z = 5.99$): This is the second highest redshift quasar known to date. The Lyα emission line is centered at ∼8500 Å, and a separate N v component is also detected. The rest-frame equivalent width of Lyα + N v is ∼60 Å. The Lyα forest is stronger than that in SDSS 0836+0054, but there is still detectable flux in the Lyα forest region, immediately blueward of the Lyα emission line. The apparent absorption at ∼9400 Å is not real but is due to imperfect telluric absorption correction in this noisy spectrum. The object has $z^* = 19.47$ and is detected at the 4 σ level in the SDSS i band. It is also a luminous object, with $M_{1450} = -26.93$ in the $\Omega = 1$ model.

SDSSp J103027.10+052455.0 ($z = 6.28$): This is the highest redshift quasar known to date. At $z^* = 20.05$ and $J = 18.87$, it is also the faintest quasar found in the current survey and has $M_{1450} = -26.89$ in the $\Omega = 1$ model. It is close to the flux limit of the survey and is only detected at 10 σ in z. The object is very red and is completely undetected in the SDSS i band. The discovery spectrum shows very strong Lyα + N v emission, with a rest-frame equivalent width of ∼70 Å, and a tentative detection of a separate N v component. The Lyα absorption is strikingly strong, with almost no detectable flux blueward of the Lyα emission. A strong C iv emission line is detected in the near-IR spectrum (Fig. 6). A Gaussian fit to the C iv line profile yields $z_{em} = 6.28 \pm 0.02$, with a rest-frame EW = 31.5 ± 8.6 Å. The continuum shape at 9000 Å $< \lambda <$ 13000 Å is consistent with $f_\nu \propto \nu^{-0.5}$, as indicated by the dashed line in Figure 6.

4.2. *Metallicity of $z \sim 6$ Quasars*

Emission-line ratios can be used to measure the metallicity of the gas in the broad emission line region (BELR). There is growing evidence from those measurements that BELR have roughly solar or higher metallicities even out to $z > 4$ (e.g., Hamann & Ferland 1999). We use the spectra of our quasars to estimate the quasar metallicity at $z \sim 6$.

Of various line ratios, N v λ1240/C iv λ1549 and N v λ1240/He ii λ1640 are particularly useful abundance diagnostics (Hamann & Ferland 1993, 1999). Hamann & Ferland (1993) examined the chemical evolution of BELR gas by applying spectral synthesis and chemical enrichment models to the N v/He ii and N v/C iv line ratios. They found that nominal BELR parameters predict N v/He ii near unity for solar abundance, increasing to ∼10 for $Z \sim 10\ Z_\odot$. The sensitivity of N v/C iv to metallicity is due to the fact that N is a secondary element, with abundance proportional to Z^2, while C is a primary element with abundance proportional to Z. Their calculations show that for the interstellar medium associated with a population with solar abundance, N v/C iv < 0.1. Luminous quasars at $2 < z < 5$ show N v/C iv ∼ 0.1–2, indicating a metallicity of $Z_\odot \lesssim Z \lesssim 10\ Z_\odot$.

From the Keck/NIRSPEC J-band spectrum of SDSS 1030+0524, we find that the rest-frame EW of C iv is 31.5 ± 8.6 Å. We do not detect He ii in emission at ∼11900 Å, which indicates that the He ii EW is smaller than ∼5 Å at 3 σ. The discovery spectra in Figure 5 show tentative detections of N v emission in all three quasars. The quality of the spectra does not allow an accurate fit to the Lyα + N v line profile in order to derive the equivalent width of N v. If we assume the EW of N v to be of the order 10 Å and a power-law continuum with $f_\nu \propto \nu^{-0.5}$, we find the flux ratios N v/C iv $\gtrsim 0.4$ and N v/He ii $\gtrsim 3.0$. Both limits would imply supersolar metallicity of the BELR region. In the calculation of Hamann & Ferland (1993), these line ratios are consistent with the "giant elliptical" model with fast stellar evolution and a top-heavy initial mass function, with $3\ Z_\odot < Z < 10\ Z_\odot$. A high-resolution, high-S/N spectrum is needed to fit the Lyα + N v line profile and put better constraints on the line ratios (Paper II). However, note that Krolik & Voit (1998) have pointed out that N v can be excited by resonance scattering from the red wing of the Lyα emission line, thus biasing these metallicity calculations.

4.3. *Average Absorption in the* Lyα *Forest Region*

The luminous high-redshift quasars discussed in this paper are ideal targets for detailed studies of the intergalactic medium at high redshift. We calculate average absorption in the Lyα forest region based on the discovery spectra. The results are summarized in Table 4, which also includes the measurements for SDSS 1044−0125. Three quantities are calculated for each quasar. We first estimate the average continuum decrements as $D_{A,B} \equiv \langle 1 - f_\nu^{obs}/f_\nu^{con} \rangle$, where f_ν^{obs} and f_ν^{con} are the observed and the unabsorbed continuum flux of the quasar and D_A and D_B measure the decrements in the region between rest-frame Lyα and Lyβ (λ = 1050–1170 Å) and between Lyβ and the Lyman limit (λ = 920–1050 Å), respectively (Oke & Korycansky 1982). Following Fan et al. (2000b), we measure D_A and D_B assuming a power-law continuum ν^α with $\alpha = -0.5$. The errors on D_A and D_B are dominated by the continuum

TABLE 4

AVERAGE Lyα ABSORPTION OF $z > 5.8$ QUASARS

Objects	Redshift	D_A	D_B	z_{abs}	Transmitted Flux Ratio at z_{abs}
J104433.04−012502.2.....	5.80	0.91 ± 0.02	0.95 ± 0.02	5.5	0.088 ± 0.004
J083643.85+005453.3.....	5.82	0.90 ± 0.02	0.91 ± 0.02	5.5	0.099 ± 0.014
J130608.26+035626.3.....	5.99	0.92 ± 0.02	0.95 ± 0.02	5.7	0.069 ± 0.014
J103027.10+052455.0.....	6.28	0.93 ± 0.02	0.99 ± 0.01	6.0	0.003 ± 0.020

determination. The error bars in Table 4 reflect the range of D_A and D_B, allowing α to range from -1.5 to $+0.5$.

The range of IGM redshifts covered by the window over which D_A is calculated is rather large ($5.0 < z_{abs} < 5.7$ for a quasar at $z = 6.0$). Therefore, we also calculate the transmitted flux ratio over a smaller window (of 0.2) centered on a redshift $z_{abs} = z_{em} - 0.3$:

$$\mathcal{T}(z_{abs}) \equiv \langle f_\nu^{obs}/f_\nu^{con} \rangle ,$$
$$(1 + z_{abs} - 0.1) \times 1216 \text{ Å} < \lambda < (1 + z_{abs} + 0.1) \times 1216 \text{ Å} . \quad (4)$$

We assume a power-law continuum of $f_\nu \propto \nu^{-0.5}$. The error bars in Table 4 reflect only the photon noise of the spectra. The quantity $\mathcal{T}$ is more noisy than D_A, but it can be calculated up to within a redshift of 0.2 of the quasar; closer than this, it would be affected both by the proximity effect from the quasar itself and by the blue wing of the Lyα emission line ($\Delta z \sim 0.2$; Oke & Korycansky 1982). In Table 4 and Figure 7, we show the $\mathcal{T}(z_{abs})$ values for the redshifts $z_{abs} \sim z_{em} - 0.3$.

From Table 4 and Figure 7, it is evident that the amount of Lyα absorption increases rapidly with redshift, with $D_A > 0.9$ at $z_{em} > 5.8$. For comparison, $D_A \sim 0.75$ at $z_{em} \sim 5$ (Songaila et al. 1999). The most striking feature, however, is that based on the spectrum of SDSS 1030+0524, $\mathcal{T}(z_{abs} = 6.0) = 0.003 \pm 0.020$, consistent with no flux detected at all. The flux level is consistent with zero from 8400 to 8700 Å in the spectrum (Fig. 5), corresponding to $5.9 < z_{abs} < 6.15$. The 1 σ *lower limit* on the flux decrement in this quasar is a factor of 50. At slightly lower redshift, we find $f/f_{con}(z_{abs} = 5.5\text{–}5.7) = 0.07\text{–}0.10$ from the other three $z > 5.8$ quasars in the sample. The flux decrement observed in SDSS 1030+0524 is at least a factor of 4 larger than that seen in any other quasar at $z > 5$. There seems to be a drastic change in the amount of Lyα absorption at $z \sim 6$.

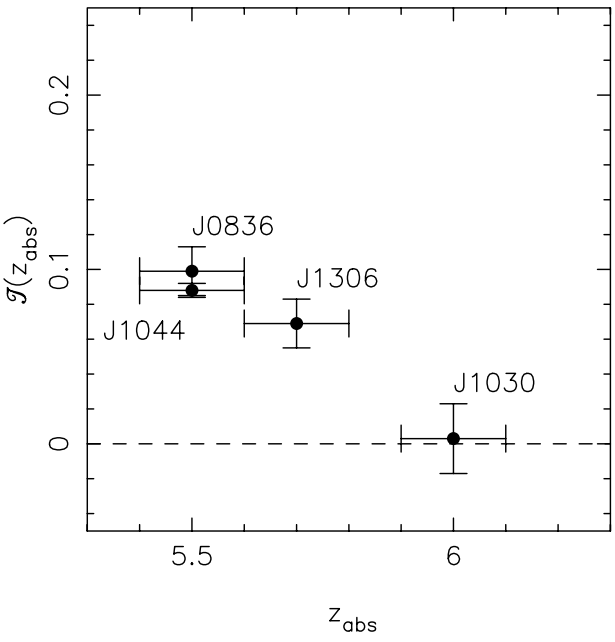

FIG. 7.—Evolution of the transmitted flux ratio in the Lyα forest region, averaged over the wavelength range $(1 + z_{abs} - 0.1) \times 1216$ Å $\lesssim \lambda \lesssim (1 + z_{abs} + 0.1) \times 1216$ Å. The vertical error bars represent the photon noise. Note that for SDSS 1030+0524, the flux is consistent with zero in the Lyα region immediately blueward of the Lyα emission.

4.4. *Gunn-Peterson Effect in the Spectrum of SDSS 1030+0524*

The absence of flux over a 300 Å region in the ARC 3.5 m discovery spectrum indicates a possible first detection of the complete Gunn-Peterson trough. This detection is still highly tentative, because of the uncertainty in sky subtraction in these low-S/N spectra. Note that spectra taken on different nights show the same nondetection of flux in the Lyα forest region. This result shows that the fraction of neutral hydrogen has increased substantially between $z = 5.7$ and $z = 6$ and, if confirmed by high-S/N spectroscopy, would show that the universe is approaching the epoch of reionization. In Paper II, we use the high-resolution Keck spectrum of SDSS 1030+0524 to place stronger constraints on the status of IGM at $z \sim 6$ and discuss its implication on the reionization of the universe in more detail.

For a uniformly distributed IGM, the Gunn-Peterson (1965) optical depth is

$$\tau_{GP}(z) = 1.8 \times 10^5 \, h^{-1} \Omega_M^{-1/2} \left(\frac{\Omega_b h^2}{0.02} \right) \times \left(\frac{1+z}{7} \right)^{3/2} \left(\frac{n_{H\,I}}{n_H} \right) . \quad (5)$$

If the IGM were mostly neutral, $n_{H\,I}/n_H \sim 1$, and the Gunn-Peterson opacity would be $\sim 10^5$. Even a tiny fraction of neutral hydrogen (of order 10^{-5}) in the IGM could result in a large optical depth and undetectable flux in the Lyα forest region. Therefore, the existence of the Gunn-Peterson trough by itself does not indicate that the object is observed prior to the reionization epoch, as it takes only a tiny fractional abundance of neutral hydrogen to create a trough. Indeed, both semianalytic models (Miralda-Escudé et al. 2000) and hydrodynamic simulations (Gnedin 2000) of structure formation show that the Gunn-Peterson trough should begin to appear at $z \sim 6$, while the epoch of overlap of H II regions could have occurred at a higher redshift.

5. SPATIAL DENSITY OF $z \sim 6$ QUASARS

5.1. *A Color-selected Complete Sample at $z > 5.8$*

The three new $z > 5.8$ quasars presented in this paper, plus SDSS 1044−0125, constitute a complete color-selected flux-limited sample of $z > 5.8$ quasars at $z^* < 20.2$. The

TABLE 5

CONTINUUM PROPERTIES OF $z > 5.8$ QUASARS IN THE COMPLETE SAMPLE

Object	Redshift	m_{1280}	m_{1450}	M_{1450} (Ω model)	M_{1450} (Λ model)	$E(B-V)$
J083643.85+005453.3.....	5.82	18.88	18.81	−27.62	−27.88	0.050
J103027.10+052455.0.....	6.28	19.73	19.66	−26.89	−27.15	0.023
J104433.04−012502.2.....	5.80	19.28	19.21	−27.15	−27.50	0.054
J130608.26+035626.3.....	5.99	19.61	19.55	−26.93	−27.19	0.028

color selection criteria are listed in equation (1), and the total sky coverage is 1550 deg^2 using the SDSS photometric runs in Table 1. The continuum properties of this sample are given in Table 5. Following Fan et al. (2000c), the quantity AB_{1280} is defined as the AB magnitude of the continuum at rest-frame 1280 Å, after correcting for interstellar extinction using the map of Schlegel, Finkbeiner, & Davis (1998). We extrapolate the continuum to rest-frame 1450 Å, assuming a continuum shape $f_\nu \propto \nu^{-0.5}$ to calculate AB_{1450}. Table 5 also lists the absolute magnitudes M_{1450} and M_{1280} in both the Λ and $\Omega = 1$ models. In the next subsections, we first calculate the selection function of our color-selected sample and then derive the total spatial density of luminous quasars at $z \sim 6$.

5.2. *Selection Function*

The selection function $p(M_{1450}, z)$ is defined as the probability that a quasar of a given M_{1450} and z will satisfy the selection criteria (eq. [1]). We calculate this using a Monte Carlo simulation of quasar colors, based on the quasar spectral model described in Fan (1999). We follow the procedures described by Fan et al. (2001a), with several modifications:

1. J-band magnitudes are included in the calculation. We use the J-band filter curve measured for the filters used in the GRIM II instrument on the ARC 3.5 m (we assume that the UFTI and MAGIC instruments have similar J-band filter curves). It is very similar to the filter used in 2MASS. The detailed filter curve is available from the authors. Since the J-band flux of the quasar is dominated by the power-law continuum, any small differences between the J-band filter curves of different instruments have little effect on the selection function.

2. SDSS photometric errors, as a function of seeing, are modeled in more detail. The selection criteria include $\sigma(z^*) < 0.10$, which is a strong function of the z^* magnitude and the observed seeing. We first construct the distribution of i and z seeing for the entire survey area. In the simulation, we randomly draw the i and z seeings from this distribution and use them to calculate the photometric error terms of the SDSS magnitudes.

3. The selection is based on the z^* magnitudes without correcting for interstellar extinction. We therefore construct the $E(B-V)$ distribution of the entire survey area based on the dust map of Schlegel et al. (1998) and assign values of $E(B-V)$ drawn at random from this distribution to the quasars in the simulation.

Following Fan et al. (2001a), we model the quasar intrinsic spectral energy distributions (SEDs) using a power-law continuum $f_\nu \propto \nu^{-\alpha}$, with $\alpha = 0.79 \pm 0.34$, plus a series of broad emission lines, with the rest-frame equivalent width of Lyα + N v with a mean of 69.3 Å and a standard deviation of 18.0 Å. We use the quasar absorption-line models in Fan (1999) to simulate the Lyα absorption, which is critical to predicting the colors of high-redshift quasars. In this model, we assume that the number density of Lyα forest lines evolves as $N(z) \propto (1+z)^{2.3}$.

The results of the selection function are summarized in Figure 8 for both cosmologies. The heavy lines in the figure represent the 5% contour, indicating the survey limit in absolute magnitude at each redshift. From the figure, we note the following:

1. The survey is sensitive to the redshift range $5.8 \lesssim z \lesssim 6.3$. The lower limit is due to the cut $i^*-z^* > 2.2$. The upper limit is due to both the cut $z^*-J > 1.5$ and the fact that quasars begin to disappear from z-band images because of Lyα absorption in the z band (§ 2.1).

2. At $5.8 \lesssim z \lesssim 6.0$, the survey reaches $M_{1450} \sim -26.5$ and is rather complete ($p > 0.8$) at the bright end. At $z > 6.0$, it becomes increasingly incomplete even for $M_{1450} < -27$. The survey limiting absolute magnitude as a function of redshift changes much faster than the change in distance modulus would indicate, because of increasing Lyα absorption in the z band.

Figure 8 also plots the locations of the four quasars in the sample. Three of them are located in the region of high selection probability ($p > 0.6$), while the highest-redshift and faintest object, SDSS 1030+0524, has a selection probability of only ~20%.

These calculations are based on the statistics of the quasar emission-line, continuum, and absorption systems observed at much lower redshift, $z \sim 4$. To test the sensitivity of our conclusions to our imperfect knowledge of quasar SEDs at $z \sim 6$, we repeated the calculations with various continuum slopes and emission-line strengths. If we assume a different slope for the power-law continuum, $\langle\alpha\rangle = 0.3$ rather than 0.79, we find that the selection probabilities of the quasars change by an average of 3%; similarly, when we change the average equivalent width of the Lyα + N v blend from 69 to 39 Å, the selection probabilities change by 2%. Thus, given the small size of the quasar sample, the error in the estimated spatial density (§ 5.3 below) is dominated by small number statistics rather than the assumptions made in the quasar color simulation. However, using these simulations we find that the selection criteria in equation (1) will not select quasars with undetectable emission lines [EW(Lyα) ~ 0, e.g., SDSS 1533−0039; Fan et al. 1999b]. Such objects will have bluer $i-z$ and redder $z-J$ colors and are located much closer to the stellar locus. They can, however, be selected using a more relaxed color cut. For example, using $i-z > 2.0$ and $z-J < 1.8$, the average selection probability of these unusual quasars will be higher than 40% for bright quasars at $z < 6.2$.

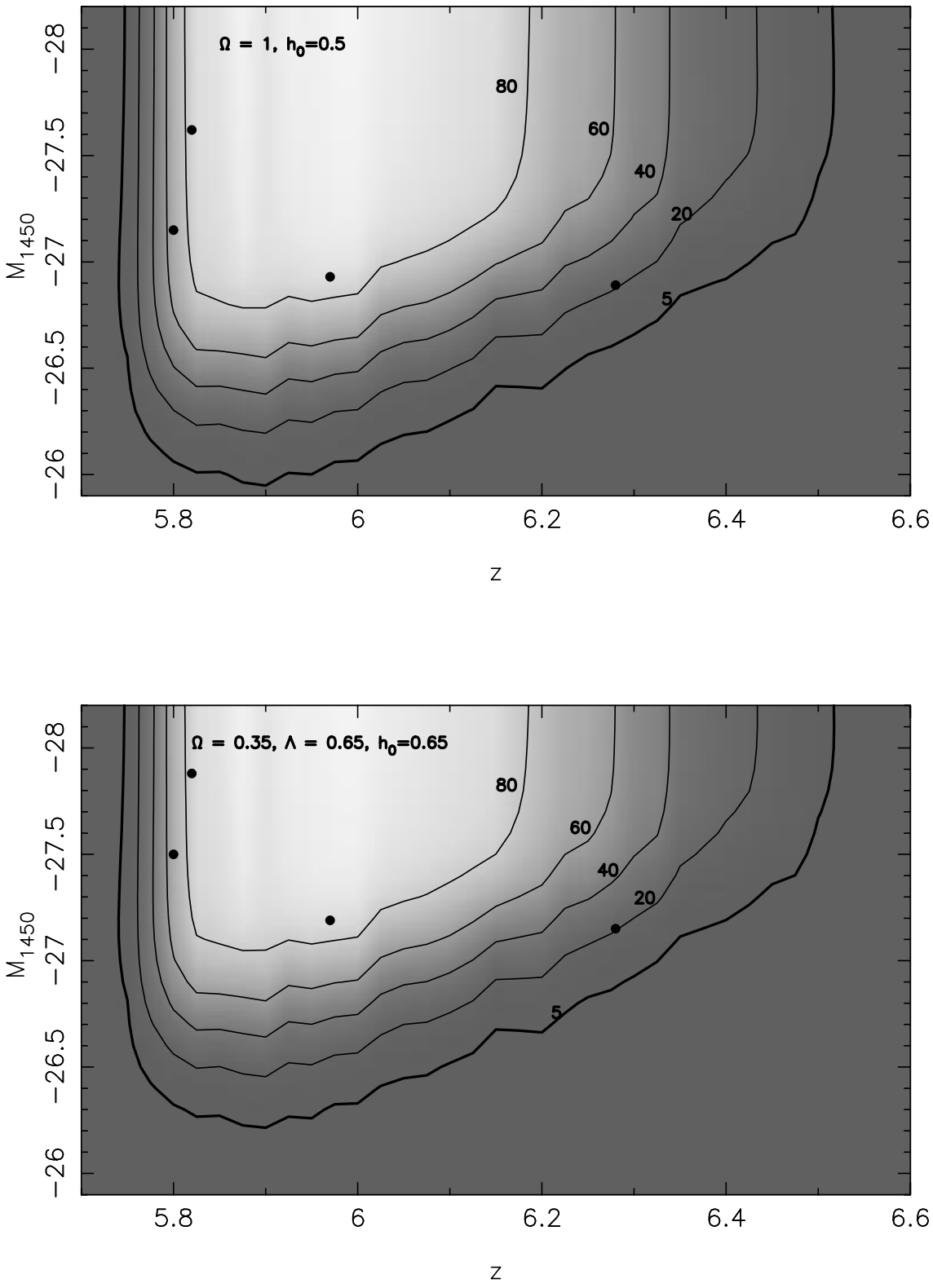

FIG. 8.—Selection probability of $z > 5.8$ quasars as a function of redshift and luminosity for the $\Omega = 1$ and the Λ models. The probability contours of 5%, 20%, 40%, 60%, and 80% are shown. The large dots represent the locations of the four quasars in the sample.

The i^*-z^* color of $z \sim 6$ quasars is mainly determined by the Lyα absorption. We have very little idea of how the Lyα forest evolves with redshift at $z \sim 6$. However, as shown in § 4.3, there is tentative evidence that the evolution of average absorption is stronger than if we assume a simple extrapolation from lower redshift. If that is the case, then at a given redshift, we will overestimate the i flux in our models, while the z flux remains almost unchanged, as it is dominated by the quasar intrinsic spectrum (continuum plus emission lines) redward of Lyα. Thus the true i^*-z^*

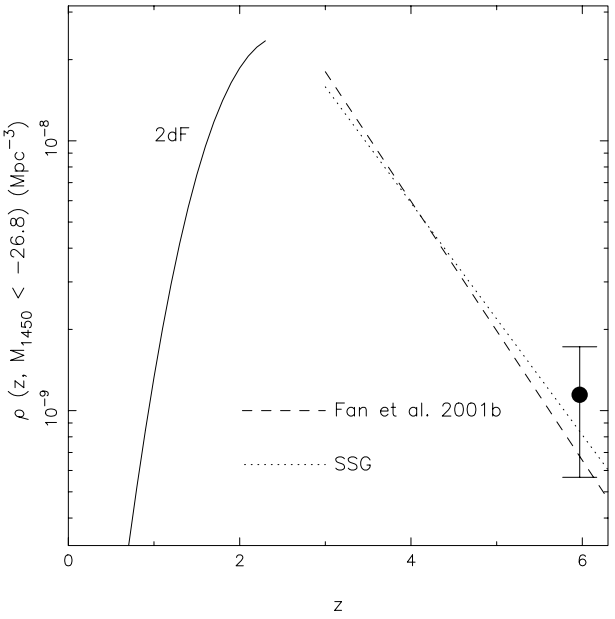

FIG. 9.—Evolution of quasar comoving spatial density at $M_{1450} < -26.8$ in the $\Omega = 1$ model. The large dot represents the result from this survey. The dashed and dotted lines are the best-fit models from Fan et al. (2001b) and Schmidt et al. (1995), respectively. The solid line is the best-fit model from the 2dF survey (Boyle et al. 2000) at $z < 2.5$.

color of quasars is redder than the model we assume here, while the z^*-J color changes little. This means that our i^*-z^* color cut would be sensitive to quasars at redshifts slightly below 5.8; the selection probability at $z > 5.8$ would remain unchanged.

The presence of foreground dust in the quasar environment would redden the quasar colors. In Figure 2, we indicate the reddening vector for $E(B-V) = 0.10$ for a quasar at $z = 6$. As discussed in Fan et al. (2001b), the number density of high-redshift quasars could be significantly affected by the uncertain amount of dust extinction.

5.3. *Spatial Density of Luminous Quasars at $z \sim 6$*

With four quasars in the sample, we can only derive the total spatial density of the quasars in the redshift and luminosity range the survey covers. We calculate this quantity using the $1/V_a$ method, following the discussion in Fan et al. (2001a). For each quasar, the volume over which it would have been observed in our survey is

$$V_a = \int_{\Delta z} p(M_{1450}, z) \frac{dV}{dz} dz , \quad (6)$$

where the integral extends over the redshift range $5.7 < z < 6.6$. The total spatial density and its statistical uncertainty can be estimated as

$$\rho = \sum_i \frac{1}{V_a^i} , \sigma(\rho) = \left[\sum_i \left(\frac{1}{V_a^i} \right)^2 \right]^{1/2} . \quad (7)$$

Using the selection function presented in § 5.1, we find that at the average redshift of $\langle z \rangle = 5.97$, $\rho(M < -26.8) = (1.14 \pm 0.58) \times 10^{-9}$ Mpc^{-3} in the $\Omega = 1$ model, and $\rho(M < -27.1) = (0.70 \pm 0.35) \times 10^{-9}$ Mpc^{-3} in the Λ-model.

Schmidt, Schneider, & Gunn (1995, hereafter SSG) derive the high-redshift quasar luminosity function in the range $2.7 < z < 4.75$ using 90 quasars at $M_{1450} \lesssim -26$. Fan et al. (2001b) calculate the evolution of the quasar luminosity function over the range $3.6 < z < 5.0$ and $-27.5 < M_{1450} < -25.5$, using a sample of 39 quasars; the two luminosity functions are in good agreement. In Figure 9, we show the density of quasars at $M_{1450} < -26.8$ found in this paper, along with the results from SSG, Fan et al. (2001b) and the 2dF survey (Boyle et al. 2000) at $z < 2.5$. The quasar density at $z \sim 6$ found in this paper is consistent with extrapolating the best-fit quasar luminosity functions in the range $3 \lesssim z \lesssim 5$ from SSG and Fan et al. (2001b). Both SSG and Fan et al. (2001b) assume a single power-law luminosity function at the bright end and that the number density of quasars declines exponentially as a function of redshift. For example, in the $\Omega = 1$ model, the maximum likelihood results of Fan et al. (2001b) find that at $z = 5$, $\rho(M_{1450} < -26.8) = 1.98 \times 10^{-9}$ Mpc^{-3}. Extrapolating the result to $z = 6$, we predict $\rho(M_{1450} < -26.8) = 0.65 \times 10^{-9}$ Mpc^{-3}, within 1 σ of the spatial density estimated in this paper. From $z = 5$ to $z = 6$, the density of luminous quasars drops by a factor of ~ 1.8. This drop is consistent with a decline of a factor of 3 per unit redshift found in Fan et al. (2001b) and 2.7 per unit redshift found in SSG.

6. DISCUSSION

At $M_{1450} \sim -27$, the luminous quasars described in this paper are likely to reside in the most massive systems at high redshift. We estimate the masses of the central black holes in these quasars following the assumptions of Fan et al. (2000c): the quasars are emitting at the Eddington luminosity with SED modeled by Elvis et al. (1994), and the fluxes of the observed quasars are not significantly magnified by gravitational lensing or beaming. We find that in the Λ-model, the estimated black hole masses are $M_{\rm BH} = 4.8 \times 10^9$, 2.0×10^9, and 1.9×10^9 $M_\odot$ for SDSS 0836+0054, 1306+0356, and 1030+0524, respectively. Under the same assumptions, $M_{\rm BH} = 3.4 \times 10^9$ $M_\odot$ for SDSS 1044−0125. In the $\Omega = 1$ model, the estimated black hole masses are about 20% lower. Note that the Elvis et al. (1994) quasar SED, which we use to estimate the (substantial) bolometric correction from the flux at rest wavelength of 1450 Å, is based on quasars at $z \lesssim 2$. The bolometric correction of quasars at $z \sim 6$ could in fact be quite different, but to determine this will require observations of these high-redshift quasars over a large range of wavelengths.

There is no established relation between black hole mass and the mass of the galactic bulge in which it resides, at high redshift. If we make the rather large assumption that the Magorrian et al. (1998) relation, $M_{\rm BH}/M_{\rm bulge} = 3 \times 10^{-3}$, determined at $z \sim 0$, also holds at high redshift, we find that in the Λ-model, $M_{\rm bulge} = (6\text{–}16) \times 10^{11}$ $M_\odot$ for the quasars in this paper. Assuming further that the ratio of the bulge to dark matter halo mass is of order the ratio of Ω_b to Ω_M, we find that these quasars reside in dark matter halos with mass $M_{\rm halo} \sim 10^{13}$ $M_\odot$ for $\Omega_b/\Omega_M \gtrsim 10$. However, Kauffmann & Haehnelt (2000) argue that the ratio of black hole mass to bulge mass could be smaller at high redshift (see also Ridgway et al. 2001). Alternatively, using the Gebhardt et al. (2000) $z \sim 0$ relation between black hole mass and bulge velocity dispersion $M_{\rm BH} = 1.2 \times 10^8$ $M_\odot$ $[\sigma_{\rm bulge}/(200$ km s$^{-1})]^{3.75}$, we find $\sigma_{\rm bulge} = 420$–530 km s^{-1}.

Note that we assume that these four high-redshift quasars are not magnified by gravitational lensing. In a $\Omega = 1$ universe, the lensing probability rises steeply with redshift up

to $z \sim 1$, then becomes rather flat. In a Λ-dominated model, the increase in lensing probability stays steep to somewhat higher redshift but flattens above the redshift at which the universe is matter dominated. Using the equations of Turner (1990), we find the raw lensing probability to be ~ 0.01 at $z \sim 6$ for reasonable assumptions for the lensing optical depth. The probability of magnification bias, however, could be much larger since the sample in this paper is a flux-limited sample, and the observed quasars are on the tail of a steep luminosity distribution (Blandford & Narayan 1992). A detailed calculation of magnification bias is beyond the scope of this paper.

Following Turner (1991) and Haiman & Loeb (2001), we consider the growth of supermassive black holes in high-redshift quasars. The *e*-folding timescale for black hole growth is $4 \times 10^7(\epsilon/0.1)\eta^{-1}$ yr, where η^{-1} is the ratio of the quasar bolometric luminosity to the Eddington luminosity, and ϵ is the radiation efficiency. For SDSS 0836+0054, the most luminous quasar in our sample, it takes 20η *e*-folding times, or ~ 0.8 Gyr, to grow from a 10 $M_\odot$ stellar black hole, if $\epsilon = 1$. This timescale is very close to the age of the universe at $z \sim 6$ in the Λ-model. If $\eta = 1$, it is actually *longer* than the age of the universe in the $\Omega = 1$ model. Note that the black hole could grow much faster if the radiation efficiency is very low. Alternatively, the black hole could have formed from a much more massive seed black hole, such as a very massive object in Population III (Bond, Arnett, & Carr 1984) or from mergers of smaller black holes (e.g., Kauffmann & Haehnelt 1999; Menou, Haiman, & Narayanan 2001).

6.1. *Constraint on the Shape of the Quasar Luminosity Function*

The quasar luminosity function at high redshift is a sensitive test of cosmological parameters and models of quasar evolution. The observed luminous quasars most probably represent rare peaks in the density field at $z \sim 6$ and, hence, probe the exponential, high-mass tail of the underlying dark matter halo distribution. The slope of the luminosity function is determined by both the slope of the halo mass function and the relation between black hole mass (proportional to quasar luminosity if the quasar is radiating at the Eddington limit) and dark halo mass. The $z \sim 6$ quasars presented in this paper are extremely rare objects, representing many-σ peaks in the density field. One would therefore expect their luminosity function to be very steep. We use the luminosity distribution of the four quasars in our sample to constrain the slope of the bright end of the quasar luminosity function and compare it with theoretical expectations, assuming that the fluxes of the four observed quasars are not significantly magnified by gravitational lensing.

Among the four quasars in the complete sample in Table 5, two have $M_{1450} < -27$ ($\Omega = 1$ model). We use this as a constraint to calculate the expected number of fainter quasars in the survey area, assuming a power-law luminosity function, $\Psi(L) \propto L^\beta$, and taking into account the survey selection function presented in Figure 8. We then compare this expected number with the actual number of lower luminosity quasars observed (two at $M_{1450} > -27$). For $\beta > -3.9$, we expect to find less than six quasars at $M_{1450} > -27$ in our survey. In this case, the probability of observing fewer than three lower luminosity quasars is larger than 5% (assuming Poisson statistics). Therefore, $\beta > -3.9$ is consistent with the observed distribution at greater than the 2 σ level. Note that this constraint encompasses the values of the bright-end slope of the quasar luminosity function from Fan et al. (2001b), who found $\beta = -2.6$ using a sample of quasars at $z \sim 4$, and Boyle et al. (2000), who found $\beta = -3.4$ at $z < 2$. However, the observed luminosity distribution is not consistent with an even steeper luminosity function. The probability drops to 0.01 for $\beta = -4.3$, and to 0.001 for $\beta = -4.6$. In other words, a steep quasar luminosity function with $L \propto L^{-4.6}$ is ruled out at the $\sim 3\,\sigma$ level by the current observations. This constraint simply reflects the fact that even after taking into account the lower selection completeness of the survey at the faint end, there are not many lower luminosity quasars in our survey at $z \sim 6$ (only two are observed), given that we have discovered two bright ones ($M_{1450} < -27$, $z^* < 19.3$). We note that this constraint on the slope of the bright end of the luminosity function is quite weak, as it is based on only four objects and depends strongly on our model of the survey selection function being reasonably correct and the assumption that the observed quasars are not significantly magnified by gravitational lensing. In order to obtain a stronger constraint on the slope of the luminosity function, a large and, more importantly, a deeper sample of $z > 6$ quasars is needed.

Is this constraint on the bright-end slope of the quasar luminosity function consistent with a simple model of quasar evolution? We can answer this question in the context of specific models of quasar formation. Following Haiman & Loeb (1998), we assume that there is a monotonic relation between quasar luminosity at high redshift and the mass of the dark matter halo in which it resides, and we assume further that every black hole shines as a quasar for a given fraction of the age of the universe to that redshift (the "lifetime" or "duty cycle" of the quasar). We can then match the observed quasar number density at $z = 6$ to the number density of dark matter halos found in the Hubble-volume simulations (Jenkins et al. 2000), if we assume that the quasars in our sample are associated with dark matter halos more massive than $M_{\rm halo} = 1\text{–}3 \times 10^{13}\ M_\odot$. In this case, the dark halo mass function at this mass scale has a logarithmic slope between -5 and -6, depending on the cosmology and quasar lifetime ($\sim 10^7$–10^8 yr). Note that this minimum halo mass is comparable to that estimated using the $z \sim 0$ relation of Magorrian et al. (1998), assuming that the quasars radiate at the Eddington limit.

These luminous quasars represent about 5 σ peaks in the density field for a Λ-CDM power spectrum, and the mass function is extremely steep at this mass. The slope of the dark halo mass function is steeper than that of the quasar luminosity function $\beta > -4.6$. This difference in the slopes of the bright end of the quasar luminosity function and the dark halo mass function at the corresponding mass scale implies that for high-redshift quasars, the luminosity L cannot simply scale linearly with $M_{\rm halo}$; rather, high-mass black holes radiate more efficiently than do lower mass ones. Alternatively, the quasar luminosity function can be shallower than the mass function if there is large scatter in the L-M relation, or if the fluxes of the observed quasars have been significantly amplified by gravitational lensing. Clearly, the above results are oversimplified and are based on a number of assumptions regarding both quasar activity and the correspondence between quasar luminosity and the mass of the dark matter halo in which it resides. However,

they illustrate the importance of the measurement of the shape of the quasar luminosity function in constraining models of quasar formation and evolution.

6.2. *Quasar Contribution to the Ionizing Background at $z \sim 6$*

The absence of the Gunn-Peterson trough in SDSS 1306+0356 ($z = 5.99$) indicates that the universe is still highly ionized at $z \sim 5.7$, presumably by the ionizing photons from quasars and star-forming galaxies. The photon emissivity per unit comoving volume required to keep the universe ionized at $z = 6$ in the $\Omega = 1$ model is

$$\dot{\mathcal{N}}_{\rm ion}(z) = 10^{51.2}\ {\rm s}^{-1}\ {\rm Mpc}^{-3}\left(\frac{C}{30}\right) \times \left(\frac{1+z}{6}\right)^3\left(\frac{\Omega_b h^2}{0.02}\right)^2 \quad (8)$$

(Madau, Haardt, & Rees 1999), where C is the clumping factor of the IGM. Based on the extrapolation of the quasar luminosity function from $z < 4.5$, Madau et al. (1999) conclude that quasars alone do not provide enough ionizing photons to keep the universe ionized at $z > 5$ and that the major contribution to the cosmic ionizing background has to be produced by star-forming galaxies (see also Steidel, Pettini, & Adelberger 2001). Here we calculate the total contribution of the quasar population to the ionizing background at $z \sim 6$, using the quasar density derived in § 5.2 and the constraint on the bright-end slope of the quasar luminosity function in § 6.1.

We calculate the total emissivity per unit comoving volume of ionizing photons from the quasar population:

$$\dot{\mathcal{N}}_{Q(z)} = \epsilon_Q^{1450}(z)/n_I^{1450}\ , \quad (9)$$

where $\epsilon_Q^{1450}(z)$ is the total quasar emissivity at 1450 Å, with units of ergs s^{-1} Hz^{-1} Mpc^{-3}, assuming a luminosity function $\Psi(L, z)$,

$$\epsilon_Q^{1450}(z) = \int \Psi(L_{1450}, z) L_{1450}\, dL_{1450}\ , \quad (10)$$

and n_I^{1450} is the total number of ionizing photons for a source with a luminosity of 1 ergs s^{-1} Hz^{-1} at 1450 Å. We assume the quasar SED following Madau, Haardt, & Rees (1999),

$$L(\nu) \propto \begin{cases} \nu^{-0.3}\ , & \text{if } 2500\ \text{Å} < \lambda < 4400\ \text{Å}\ , \\ \nu^{-0.8}\ , & \text{if } 1050\ \text{Å} < \lambda < 2500\ \text{Å}\ , \\ \nu^{-1.8}\ , & \text{if } \lambda < 1050\ \text{Å}\ , \end{cases} \quad (11)$$

and integrate over the energy range from 1 to 4 ryd, with a cutoff at 4 ryd because of He II absorption.

We assume that the luminosity function of quasars at $z \sim 6$ is described by a double power law and write it as a function of absolute magnitude M_{1450}:

$$\Psi(M_{1450}) = \frac{\Psi^*}{10^{0.4(\beta_1+1)(M_{1450}-M_{1450}^*)} + 10^{0.4(\beta_2+1)(M_{1450}-M_{1450}^*)}}\ , \quad (12)$$

where M_{1450}^* is the characteristic luminosity. None of the current quasar surveys at $z > 4$ constrains the faint-end slope of the quasar luminosity function. For example, Fan et al. (2001b) only compute the luminosity function at $M_{1450} < -25.5$. Therefore, the characteristic luminosity M_{1450}^* and the faint-end slope β_2 are both unknown at high redshift, and we simply *assume* the faint-end slope of the luminosity function to be the same as determined by Boyle et al. (2000) at $z < 2$, $\beta_2 = -1.58$. Thus, for a given bright-end slope β_1, we can derive Ψ^* by requiring $\int_{-\infty}^{-26.8} \Psi(M) dM = 1.1 \times 10^{-9}$ Mpc^{-3}, as determined in § 5.2.

In § 6.1, we demonstrated that the bright-end slope β_1 of the quasar luminosity function at $z \sim 6$ is consistent with that measured at lower redshift ($\beta_1 = -2.58$, Fan et al. 2001b; $\beta_1 = -3.43$, Boyle et al. 2000), and that a much steeper slope can be ruled out ($\beta_1 < -4.3$ is ruled out at the 99% confidence level, and $\beta_1 < -4.6$ with 99.9% confidence). In Figure 10, we calculate the quasar ionizing photon density integrated over the full luminosity function as a function of M_{1450}^* for a series of values of β_1, assuming $\beta_2 = -1.58$ and normalizing to the quasar density at $M_{1450} < -26.8$. The quasar ionizing photon density is compared with what is required to keep the universe ionized at $z \sim 6$ (*heavy solid line*).

From Figure 10, it is evident that with $\beta_1 > -3.5$, quasars would not produce enough photons to keep the universe ionized at $z \sim 6$ unless $M_{1450}^* > -23$; i.e., only if the ionizing background is dominated by low-luminosity AGNs can the quasar luminosity function provide enough ionizing photons. This would imply a large negative luminosity evolution of the luminosity function. The universe could be ionized with luminous quasars only if the bright-end slope of the luminosity function were much steeper than that measured at low redshift; but such a steeper slope is

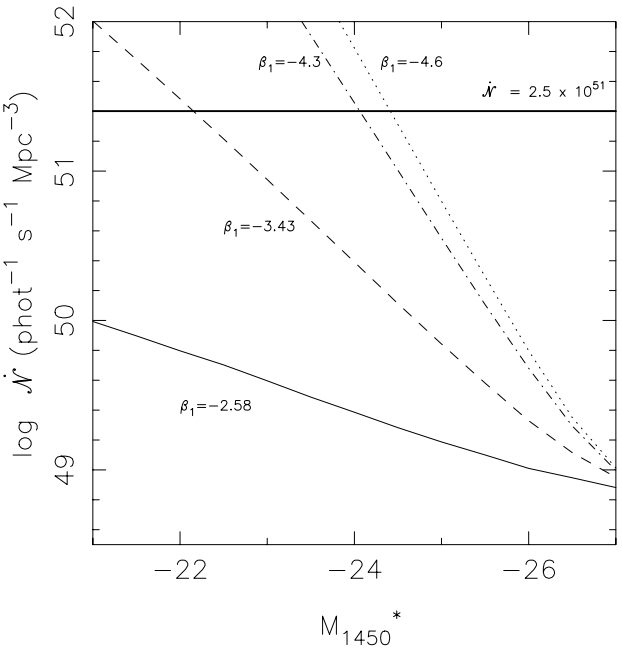

FIG. 10.—Comoving emission density rate of hydrogen Lyman continuum photons from quasars integrated over the full luminosity function, compared with the minimum rate (*heavy solid line*) that is needed to fully ionize a universe at $z = 6$ in the $\Omega = 1$ model, with a clumping factor of 30 and the baryon fraction $\Omega_b h^2 = 0.02$. The recombination time is assumed to be faster than the Hubble time. The quasar emission rate is calculated for different bright-end slopes of the quasar luminosity function (β_1) and turnover luminosity M_{1450}^*, assuming the same faint-end slope $\beta_2 = -1.58$ and the total density of luminous quasars matched to that found in this paper, $\rho(z = 6, M_{1450} < -26.8) = 1.14 \times 10^{-9}$ Mpc^{-3}.

not consistent with our sample. This calculation underlines the importance of searching for faint quasars and studying the shape of the high-redshift quasar luminosity function at the low-luminosity end. While it is unlikely that quasars provide the majority of photons that ionized the universe at $z \gtrsim 6$, it still remains an open question.

7. SUMMARY

In this paper, we present three new quasars at $z > 5.8$, selected from ~ 1550 deg^2 of multicolor imaging data from the Sloan Digital Sky Survey. The quasar candidates are selected as i-dropout objects with red $i^* - z^*$ colors. They are separated from red cool dwarfs using follow-up J-band photometry. The three new quasars, with redshifts of 5.82, 5.99, and 6.28, are the highest-redshift objects with spectral confirmation known to date.

The spectra of the new quasars show very strong Lyα absorption blueward of the Lyα emission, with more than 90% of the flux absorbed. The amount of absorption increases rapidly toward $z_{\rm abs} \sim 6$. For the $z = 6.28$ quasar SDSS 1030+0524 the flux is consistent with zero in a region of 300 Å immediately blueward of Lyα emission. It suggests a tentative detection of a complete Gunn-Peterson trough, indicating that at $z \sim 6$ the universe is close to the reionization epoch.

The discovery spectra show tentative detection of the N V emission line, suggesting the existence of large amount of heavy metals in the gas around the quasars. A J-band spectrum of SDSS 1030+0524 shows strong C IV emission. The limits on the N V/C IV and N V/He II line ratios are consistent with the gas around the quasar having supersolar metallicity.

The three new quasars described in this paper, plus the $z = 5.8$ quasar SDSS 1044−0125 (Fan et al. 2000c), form a complete color-selected, flux-limited sample at $z \sim 6$. We calculate the color selection completeness of this sample and derive the spatial density of luminous quasars at $z \sim 6$, $\rho(M_{1450} < -26.8) = 1.1 \times 10^{-9}$ Mpc^{-3}, for $\Omega = 1$ and $H_0 = 50$ km s^{-1} Mpc^{-1}. This density is about a factor of 2 lower than that at $z \sim 5$ and is consistent with an extrapolation of the observed redshift evolution of quasars at $3 < z < 5$.

Using the luminosity distribution of the sample, we show that the luminosity function is shallower than $\Psi(L) \propto L^{-4.6}$ at the bright end. A larger and deeper sample is needed to better constrain the shape of the quasar luminosity function. We confirm that the quasar population is unlikely to provide enough photons to ionize the universe at $z \sim 6$, unless the luminosity function is much steeper than $\beta_2 = -1.58$ at the faint end.

The black hole masses of these quasars are probably several times $10^9\ M_\odot$. The quasars are likely to reside in very massive systems, with the minimum mass of host dark halos $\sim 10^{13}\ M_\odot$. These massive dark halos represent rare peaks in the density field at high redshift and are in the steep tail of the mass function, with a slope that is appreciably steeper than that of the quasar luminosity function.

Follow-up observations of the luminous high-redshift quasars described in this paper will provide excellent probes of galaxy formation and IGM evolution at high redshift. In Paper II, we present high-resolution, high-S/N optical spectroscopy of these quasars. These observations are compared with detailed cosmological simulations to constrain models of reionization in Fan et al. (2001c). X-ray observations (e.g., Brandt et al. 2001) will reveal the status of the environment very close to the quasar central engine; follow-up IR spectroscopy can provide more diagnostics on the metallicity of the quasars and reveal the possible existence of strong associated absorption (e.g., Maiolino et al. 2001); and detections of the sources at submillimeter wavelengths will shed light on the possible connections between quasar activity and starbursts (e.g., Carilli et al. 2001).

The total area of the SDSS is 10,000 deg^2. Assuming the quasar luminosity function of Fan et al. (2001b) and normalizing it to have the spatial density at $z \sim 6$ found in this paper, we expect to detect *one* $z \sim 6.6$ quasar with $z^* \sim 20$ ($M_{1450} \sim -28$) in the entire survey. A quasar at this redshift has $i^* - z^*$ and $z^* - J$ colors similar to those of early T dwarfs. This is the highest redshift of objects we expect to find using solely SDSS imaging data.

The Sloan Digital Sky Survey (SDSS) is a joint project of the University of Chicago, Fermilab, the Institute for Advanced Study, the Japan Participation Group, Johns Hopkins University, the Max-Planck-Institut für Astronomie, the Max-Planck-Institut für Astrophysik, New Mexico State University, Princeton University, the US Naval Observatory, and the University of Washington. Apache Point Observatory, site of the SDSS telescopes, is operated by the Astrophysical Research Consortium. Funding for the project has been provided by the Alfred P. Sloan Foundation, the SDSS member institutions, the National Aeronautics and Space Administration, the National Science Foundation, the Department of Energy, the Japanese Monbukagakusho, and the Max Planck Society. The SDSS Web site is http://www.sdss.org. This publication makes use of data products from the Two Micron All Sky Survey, which is a joint project of the University of Massachusetts and the Infrared Processing and Analysis Center/California Institute of Technology, funded by NASA and NSF. We thank the staff at APO, Keck, Calar Alto, and UKIRT, for their expert help, Gemini staff scientist Marianne Takamiya for carrying out the Gemini/NIRSPEC service observation. We thank Ed Turner, Peng Oh, Julian Krolik, Kristian Finlator, John Bahcall, and an anonymous referee for helpful discussions and comments. We acknowledge support from NSF grant PHY 00-70928 and a Frank and Peggy Taplin Fellowship (X. F.), NSF grant AST 00-71091 (M. A. S.), and NSF grant AST 99-00703 (D. P. S.).

REFERENCES

Anderson, S., et al. 2001, AJ, 122, 503
Becker, R. H., Gregg, M. D., Hook. I. M., McMahon, R. G., White, R. L., & Helfand, D. J. 1997, ApJ, 479, L93
Becker, R. H., et al. 2001, AJ, 122, 2850 (Paper II)
Becker, R. H., White, R. L., & Helfand, D. J. 1995, ApJ, 450, 559
Blandford, R. D., & Narayan, R. 1992, ARA&A, 30, 311
Bond, J., R., Arnett, W. D., & Carr, B. J. 1984, ApJ, 280, 825
Boyle, B. J., Shanks, T., Croom, S. M., Smith, R. J., Miller, L., Loaring, B., & Heymans, C. 2000, MNRAS, 317, 1014
Brandt, W. N., Guainazzi, M., Kaspi, S., Fan, X., Schneider, D. P., Strauss, M. A., Clavel, J., & Gunn, J. E. 2001, AJ, 121, 591
Burgasser, A. J., et al. 1999, ApJ, 522, L65
Carilli, C. L., et al. 2001, ApJ, 555, 625
Cen, R., & Haiman, Z. 2000, ApJ, 542, L75
Djorgovski, S. G., Castro, S. M., Stern, D., & Mahabal, A. 2001, ApJ, 560, L5
Elvis, M., et al. 1994, ApJS, 95, 1
Fan, X. 1999, AJ, 117, 2528

Fan, X., et al. 1999a, AJ, 118, 1
———. 1999b, ApJ, 526, L57
———. 2000a, AJ, 119, 1
———. 2000b, AJ, 119, 928
———. 2000c, AJ, 120, 1167
———. 2001a, AJ, 121, 31
———. 2001b, AJ, 121, 54
———. 2001c, AJ submitted
Finlator, K., et al. 2000, AJ, 120, 2615
Fukugita, M., Ichikawa, T., Gunn, J. E., Doi, M., Shimasaku, K., & Schneider, D. P. 1996, AJ, 111, 1748
Geballe, T. R., et al. 2001, ApJ, in press
Gebhardt, K., et al. 2000, ApJ, 539, L13
Gnedin, N. 2000, ApJ, 535, 530
Goodrich, R. W., et al. 2001, ApJ, 561, L23
Gunn, J. E., & Peterson, B. A. 1965, ApJ, 142, 1633
Gunn, J. E., et al. 1998, AJ, 116, 3040
Haiman, Z., & Loeb, A. 1998, ApJ, 503, 505
———. 1999, ApJ, 519, 479
———. 2001, ApJ, 552, 459
Hall, P., et al. 2001, in preparation
Hamman, F., & Ferland, G. 1993, ApJ, 418, 11
———. 1999, ARA&A, 37, 487
Jenkins, A., Frenk, C. S., White, S. D. M., Colberg, J. M., Evrard, A. E., Couchman, H. M. P., & Yoshida, N. 2001, MNRAS, 321, 372
Kauffmann, G., & Haehnelt, M. 2000, MNRAS, 311, 576
Krauss, L., & Turner, M. 1995, Gen. Relativ. Gravitation, 27, 1137
Krolik, J., & Voit, M. 1998, ApJ, 497, L5
Leggett, S. K., et al. 2000, ApJ, 536, L35
———. 2001, ApJ, in press
Lupton, R. H., Gunn, J. E., Ivezic, Z., Knapp, G. R., Kent, S. M., & Yasuda, N. 2001, in Proc. ADASS X, in press (astro-ph/0101420)
Lupton, R. H., Gunn, J. E., & Szalay, A. 1999, AJ, 118, 1406
Madau, P., Haardt, F., & Rees, M. J. 1999, ApJ, 514, 648
Madau, P., & Rees, M. J. 2000, ApJ, 542, L69
Magorrian, J., et al. 1998, AJ, 115, 2285
Maiolino, R., Mannuccci, F., Baffa, C., Gennari, S., & Oliva, E. 2001, A&A, 372, L5
McLean, I. S., et al. 1998, SPIE, 3354, 566
Menou, K., Haiman, Z., & Narayanan, V. K. 2001, ApJ, 558, 535
Miralda-Escudé, J., Haehnelt, M., & Rees, M. J. 2000, ApJ, 530, 1
Oke, J. B., & Korycansky, D. G. 1982, ApJ, 255, 11
Ostriker, J. P., & Steinhardt, P. 1995, Nature, 377, 600
Persson, S. E., Murphy, D. C., Krzeminski, W., Roth, M., & Rieke, M. J. 1998, AJ, 116, 2475
Richards, G. T., et al. 2001a, AJ, 121, 2308
———. 2001b, in preparation
Ridgway, S. E., Heckman, T. M., Calzetti, D., & Lehnert, M. 2001, ApJ, 550, 122
Scheuer, P. A. G. 1965, Nature, 207, 963
Schlegel, D. J., Finkbeiner, D. P., & Davis, M. 1998, ApJ, 500, 525
Schmidt, M., Schneider, D. P., & Gunn, J. E. 1995, AJ, 110, 68 (SSG)
Schneider, D. P., et al. 2000, PASP, 112, 6
Schneider, D. P., et al. 2001, AJ, 121, 1232
Shklovsky, I. S. 1964, Astron. Zh. 41, 408
Skrutskie, M. F., et al. 1997, The Impact of Large-Scale Near-IR Sky Surveys, ed. F. Garzón, N. Epchtein, A. Omont, B. Burton, & P. Persei (Dordrecht: Kluwer), 25
Songaila, A., Hu, E. M., Cowie, L., & McMahon, R. G. 1999, ApJ, 525, L5
Steidel, C. C., Pettini, M., & Adelberger, K. 2001, ApJ, 546, 665
Stoughton, C., et al. 2001, AJ, in press
Strauss, M. A., et al. 1999, ApJ, 522, L61
Tsvetanov, Z. I., et al. 2000, ApJ, 531, L61
Turner, E. L. 1990, ApJ, 365, L43
———. 1991, AJ, 101, 5
York, D. G., et al. 2000, AJ, 120, 1579
Zheng, W., et al. 2000, AJ, 120, 1607